UNIVERSITY OF BIRMINGHAM

INVESTIGATION OF Zr-BASED AMORPHOUS ALLOY MEMBRANES FOR HYDROGEN PURIFICATION

By:

Richard Wyse

A thesis submitted to
the School of Metallurgy and Materials
for the Degree of Master of Research

School of Metallurgy and Materials
University of Birmingham
Birmingham
B15 2TT
United Kingdom
September 2013

Abstract

This project focused on the fabrication and characterization of zirconium-copper and zirconium-copper-titanium amorphous alloys as hydrogen purification membranes.

Binary ribbons of Zr55Cu45 and Zr58Cu42 (wt%) ($Zr_{46}Cu_{54}$ and $Zr_{49}Cu_{51}$ at% respectively) were fabricated by melt spinning. DSC analysis determined the thermal behaviour of each ribbon under argon and hydrogen gases at 3 bar. Both ribbons exhibited similar DSC profiles including a typical crystallization peak under hydrogen at 263.9 °C and 302.9 °C respectively, but also exhibited an additional exothermic reaction around 162.7 °C and 123.3 °C respectively, also under hydrogen. XRD analysis as well as hydrogen solubility measurements showed the lower temperature peak was not crystallization or hydrogenation but an alteration of the crystal structure and stress relaxation event. The ability for both membranes to increase hydrogen uptake with increasing temperature at various pressures was demonstrated. The higher hydrogen solubility of the second binary (Zr58Cu42 wt% / $Zr_{49}Cu_{51}$) sample, in comparison to the first binary sample, was attributed to either a lower copper content and/or a lower degree of crystallinity.

A ternary ribbon Zr33Cu59Ti8 wt% ($Zr_{25}Cu_{64}Ti_{11}$ at%) was also fabricated by melt spinning to investigate the addition of Ti to a Zr-Cu based alloy. DSC measurements showed a similar thermal profile to the binary alloys, including

the stress relaxation event at lower temperature (152.4 C). The ternary sample exhibited a lower crystallization temperature in comparison to both the binary alloys under hydrogen. In-situ XRD analysis suggested that although Ti addition may promote the formation of an amorphous phase, it has a tendency to reduce the thermal stability of the alloys.

Acknowledgments

I would like express personal gratitude to a number of people who have helped me throughout this post-graduate degree, all in different ways.

Firstly I wish to thank my supervisor Dr. David Book who allowed me the freedom of subject choice and showed his continual support throughout the experience in any area I needed.
Also to Dr. Shahrouz Nayebossadri, whose experimental knowledge, tuition and input have been a great help in shaping this work and improve my skills as a researcher.

A special mention to Dr. Lydia Pickering who at the initial stages of my degree showed immense patience, generosity of time and knowledge to get me started.
This thanks continues to the greatest post-graduate class ever assembled, Luke, Claire, Josh, Rich, Lydia, Matt, Meakin, Nick, Kyle, Sheng and Simon, all who made the experience ever more fun and enjoyable.

Furthermore, much gratitude to Luke 'Hughsey' Hughes, Craig 'Knaggsy' Knaggs, Jonathan 'Kobza' Boukhobza and Dean 'Wellsy' Welton for their invaluable input and friendship throughout, who made the tough times better and the good times great.

Lastly, my Mother and Father whose love and encouragement was unwavering and my brother and sister whose insight, support and shared experience helped me get the most out of my degree.

Table of Contents

1. Introduction

Currently more than 87% of global energy is sourced from fossil fuels and demand is increasing at 5.6% pa (BP Sustainability Review 2012). These fuel resources are considered to be finite and, including the recent promising discovery of shale gas sources in the USA (Armor 2013), are generally becoming increasingly costly to discover and extract.

Estimates on depletion of conventional production of these fossil fuels are: 54 years for oil, 63 years for gas, and 112 years for coal (BP Sustainability Review 2012).

The cost and limited availability of these resources, coupled with the harmful effects of fossil fuel emissions in contributing to air pollution and global warming, has driven the demand for cleaner, greener and more efficient renewable energy sources. Therefore, there is a massive investment into alternative technologies for energy production, including wind, solar, tidal, geothermal; and into alternative means of storing and distributing energy, such as hydrogen-based technologies (BP Sustainability Review 2012). As an example of what is currently being achieved in 2011, 20% of Germany's power came from renewable energy (Spiegel Online 2011).

Currently there are numerous wide-ranging technological, logistical, infrastructure-based and cost obstacles specific to each different energy

production method (e.g. tidal, wind power, solar) that need to be individually addressed before the implementation of each renewable energy resource can contribute in replacing fossil fuels.

Hydrogen, however, is a versatile and abundant energy vector, which may prove to be viable in renewable energy production. Whether used as an energy vector, or as a storage medium, there is a large market potential for the use of hydrogen in different energy sectors.

One of the principal methods of producing hydrogen is Steam Methane Reforming (SMR) of natural gas, but residual greenhouse gases and impurities need to be eliminated from the hydrogen produced to avoid degrading the downstream processes and catalysts (Ockwig and Nenoff 2007). This purification process is essential, with the different applications determining the degree of purification needed, and it drives the need for low-cost, high-efficiency purification technologies.

A major application is the automobile industry. Rather than use it as a combustible fuel at a low degree of purification, hydrogen at a very high degree of purification can be used, by combination with oxygen, to release its chemical energy using a PEM (Proton Exchange Membrane) fuel cell to produce electricity.

A major issue with using hydrogen in this application is the need for extreme purity (99.99999%), enabling maximum efficiency of converting hydrogen into a power source.

Pressure Swing Adsorption (PSA) and Cryogenic Distillation (CD) processes are widely used in industry to produce purities ranging from 85 - 99.99% (Phair and Badwal 2006). Hydrogen Separation Membranes (HSM) however, have also been highlighted by many studies (Adhikari and Fernando 2006, Nenoff et al. 2006, Sholl and Ma 2006, Phair and Badwal 2006) to be able to produce extremely pure hydrogen (99.9999%) (Phair and Badwal 2006) for the use in automotive PEM fuel cells. However, PSA and CD are currently being installed on larger scales enabling larger volumes of hydrogen to be purified (Phair and Badwal 2006). Capital costs of these processes are inherently greater than membrane assemblies and the use of each hydrogen production source needs to be related to the application it is being used for in terms of cost, purification and sustainability.

The current industry-standard hydrogen purification membranes are crystalline Pd-based alloys, chosen for their high selectivity for hydrogen (Ockwig and Nenoff 2007). Currently Pd-based membranes are expensive and can display issues with hydrogen embrittlement at temperatures below 300 °C in the presence of hydrogen unless alloyed with silver or copper (Ockwig and Nenoff 2007, Dolan et al. 2006, Sholl and Hao 2011). Transition metal based amorphous membranes are potential alternatives that may reduce material cost and combat concerns over durability and hydrogen embrittlement (Dolan et al. 2006).

While pure Pd membranes utilize natural selectivity through their crystalline structure for hydrogen purification at temperatures up to 1000 °C (Prosperi 2006), they are less effective at low temperatures due to a combination of alpha

and beta phases forming below 300 °C (Ockwig and Nenoff 2007). Pd-Ag and Pd-Cu membranes can operate below this temperature but still prove to be an expensive material combination. Amorphous alloy membranes have the potential to use the lack of long-range order (LRO) in their crystal structure and improved resistance to hydrogen embrittlement to purify hydrogen and so be used with PEM fuel cells.

This project investigated the characteristics of two amorphous metallic-alloy systems, Zr-Cu and Zr-Cu-Ti as hydrogen separation membranes at temperatures below 500 °C.

2. Literature Review

2.1. The Hydrogen Economy

2.1.1 Availability

Hydrogen is potentially one of the most abundant energy vectors on the planet; however, it is rarely found in its pure form and is usually coupled with other substances (e.g. in the form of water, hydrocarbons, biomass, etc). The technological problems of sourcing, synthesizing, purifying, storing and delivering hydrogen energy therefore constitute major barriers to its implementation as an energy vector. However, the absence of harmful emissions (depending on how the hydrogen is produced), justifies the continued development of technologies to solve these problems.

The hydrogen economy involves producing hydrogen either on a large scale by Steam Methane Reforming (SMR) or at smaller scales by renewable sources to create a sustainable energy system. Clean hydrogen energy can be used as an energy vector or storage medium for hydrogen fuel cells — used as stationary power sources for home /industry and mobile sources for transportation — and may help to overcome the problem of intermittency associated with renewable energy sources such as wind, solar and tidal power.

With many of the world's developed countries signed up to the Kyoto Agreement, greenhouse gas emission reduction programmes have been put in place to try to reduce emissions between 2008 and 2012 to, on average, 5.2 % lower than the 1990 levels and by 80% by 2050 (Kyoto Protocol Memo 2003). This acts as a driving force for green energy production in a number of the world's leading economies.

2.1.2. Production Techniques

Steam Methane Reforming (SMR) of natural gas producing synthesis gas is currently one of a number of methods, that may become a carbon free energy source beyond 2050 (McKinsey Report 2 (NO DATE). However, SMR produces CO_2 as a product of the reaction and so needs CO_2 Capture and Storage (CCS) to reduce these emissions further.

Methane and steam react to produce hydrogen and carbon monoxide at temperatures 700–850 °C at pressures within the range 3–25 bar. The resultant CO can be further processed into more hydrogen (and CO_2) using the water gas shift (WGS) process at 250 - 450 °C (Ockwig and Nenoff 2007, Riis et al. 2006, Phair and Badwal 2006). This process still produces a large amount of CO_2, which is counter-productive in the respect of improving local air pollution when the products of this reaction are to be used in a technology that aims to reduce carbon emissions. This is where CCS technology can aid in reducing CO_2 emissions: more information on the specific technological requirements can be found in (Rubin et al. 2005).

Initial Reforming Reaction:

$$CH_4 + H_2O \leftrightarrow CO + H_2 \quad (1)$$

Water Gas Shift (WGS):

$$CO + H_2O \rightarrow CO_2 + H_2 \quad (2)$$

Steam Methane Reforming (SMR):

$$CH_4 + 2H_2O \rightarrow CO_2 + 4H_2 \quad (3)$$

Reducing the carbon emissions is a major concern in the hydrogen production process to make it a more sustainable and cleaner option.

Not only do the production techniques have a requirement to produce hydrogen with a reduced carbon footprint compared to the fossil fuel, they must also provide significant improvements in energy security or else there is little point in undertaking the process in production terms.

A move to using more renewable resources rather than fossil fuels may be a solution to reducing the carbon footprint of hydrogen production. However, in

America for example, the input of energy from hydro-electricity, geothermal, solar/PV, wind and biomass would need to reach over 6 times the current values to match that provided by current fossil fuel production options. (Monthly Energy Review DOE August 2013).

Therefore, finding hydrogen separation techniques for hydrogen production membrane reactors that are highly efficient, to maximize the potential of renewable hydrogen sources while being a cost effective method, are highly sought after to meet the volumes currently produced by fossil fuels. There are three main industry-used separation techniques: Pressure Swing Absorption, Cryogenic Distillation and Membrane Separation.

2.1.3 Separation Techniques

Pressure Swing Absorption (PSA) is the most widely used technique to separate hydrogen from a mixture of gases in industry at present. It has the advantage of operating at ambient temperatures and can produce hydrogen of purity 99.99% (Adhikari and Fernando 2006).

PSA is a large scale, stationary and mature technology that involves pressurizing gases, which causes them to selectively adsorb on the surface of certain porous materials, e.g. zeolite, or activated carbon. Increasing the pressure increases the volume of gas that can be adsorbed. Reducing the gas pressure then has the reverse effect and the gas is desorbed or released from the solid surface. (Adhikari and Fernando 2006).

This separation of hydrogen from other gases occurs as different gases are adsorbed at different temperatures. Selected porous solids can be used to only adsorb hydrogen before the residual gases are then removed before the hydrogen is then desorbed. However, this process requires pressures greater than 100 bar and so is therefore generally considered energy intensive and only produces purity up to 95% depending on impurity levels and hydrogen concentration (Phair and Badwal 2006).

Cryogenic Distillation (CD) is another well-known hydrogen separation process. CD differs from PSA in that it separates substances in the liquid form at cryogenic temperatures by utilizing the differing boiling points of the feed components. CD is a low-temperature process that consumes a large amount of energy, which can range from £24 - £1110 per tonne for nitrogen separation depending on the scale (Hinchcliffe and Porter 2000), and can only produce hydrogen in the purity range of <= 95%. Considering the need for near absolute pure hydrogen (99.9999999%) in PEM this technique proves to be impractical when used on its own (Hinchcliffe and Porter 2000).

Separation Membranes are currently at the forefront of hydrogen separation development due to their flexibility and resulting high to extremely high, purities of specific gases at relatively low pressures, 28 bar. (Phair and Badwal 2006). Polymeric membranes operate between 100 – 200 °C, dense metal membranes operate between 300 – 600 °C and porous glassy membranes can operate up to 850 °C (Phair and Badwal 2006). However, in the parameters of this study, low

temperature (300 °C and below) hydrogen separation is of most interest, potentially in conjunction with supply hydrogen for PEM fuel cells.

Porous membranes and dense metal membranes hold a number of advantages compared to PSA and CD including their ability to be operated easily, low energy consumption, reduced initial investment costs (dependent on material used) and can prove to be financially viable even for low gas volumes (Spillman 1989).

2.2. Fuel Cells

2.2.1 The Fuel Cell

Hydrogen Fuel Cells are already in use in many prototype automobiles such as the Honda Clarity FCX (Eberhard and Tarpenning 2007). They demonstrate the potential of hydrogen as a realistic alternative fuel to petroleum by using it in a hybrid system (electric motor and 100kW Honda Vertical Flow hydrogen stack fuel cell) to reduce the carbon emissions of the vehicle or as a range extender. As previously mentioned the automobile market is a potentially large market for hydrogen-based technology and so separation membranes may potentially be in great demand.

The Proton Exchange Membrane Fuel Cell (PEMFC) is currently one of the most promising types of fuel cell that is being developed for the automotive industry. Advantages of this technology include a rapid start up, working at low temperatures (80 – 100 °C (Marban and Valdes-Solis 2007)) and simple fixed

geometry compared to conventional combustion engines. This leads it to being flexible in design for different types of vehicle and suited to an automotive application. Disadvantages that accompany PEMFC include high cost (Marban and Valdes-Solis 2007, Ockwig and Nenoff 2007), due to platinum being used as the catalyst on the proton exchange membrane (PEM) surface, as well as the critical need for pure hydrogen (99.9999999% (Ockwig and Nenoff 2007)) as the energy source. PEMFC's can also be affected by impurities such as CO and H_2S (Dolan et al. 2006) poisoning the fuel cell itself by "surface blocking" or causing a "reduction in the number of approachable pathways without an energy barrier" in Pd-based alloys (Dolan et al. 2006).

PEM fuel cells principally work on the principle of reverse electrolysis. Hydrogen and oxygen combine to produce water and release electrons for power generation.

Reverse electrolysis:

$$2H_2 + O_2 \rightarrow 2H_2O \qquad (7)$$

The assembly of a PEM is depicted in Figure (1).

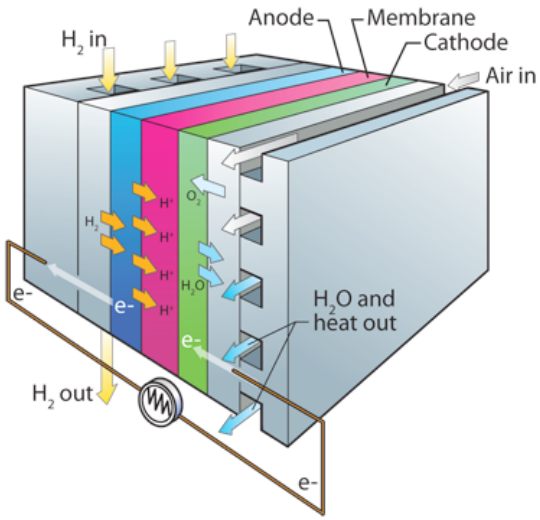

Fig. 1 Typical PEM assembly (Patterson 2011)

The cell is comprised of five layers and three main components.

The central component is a polymer electrolyte membrane (PEM). This allows only positive ions (H^+) to be transported across the PEM from the anode to the cathode to react with oxygen to form water. The electrons are unable to diffuse through the membrane and are conducted to the cathodic side via an external circuit to provide power.

Anode reaction:

$$H_2 \rightarrow 2H^+ + 2e^- \quad (8)$$

Cathode reaction:

$$O_2 + 4H^+ + 4e^- \rightarrow 2H_2O \quad (9)$$

2.2.2 Hydrogen Supply for Fuel Cells

Currently there are a number of issues concerning the performance of PEM fuel cells due to the purity of hydrogen provided to them. These include PEM surface poisoning by impurity gases, such as CO and H_2O (Dolan et al. 2006) and embrittlement of the PEM (Ockwig and Nenoff 2007). Economical concerns also include trying to improve hydrogen permeability and lower cost due to the use of Palladium (Pd) or Palladium-Silver (PdAg) as the PEM with platinum as the catalyst layer. Palladium offers near perfect selectivity for hydrogen and can operate at high temperatures up to 1000 °C, robust in catalytic membrane reactors (Dolan et al. 2006, 2009). The cost of using palladium (£170 for one 50 mm x 50 mm, 0.025 mm thick foil, compared to £72 for the same sample size of Zirconium foil (www.goodfellows.com)) however, is a barrier to this technology being financially economic to be mass-produced in the automotive industry.

Finding an alternative to a palladium-based PEM that has comparable permeability values and produces extremely high purity hydrogen (99.9999 %+) is the current technological challenge (Ockwig and Nenoff 2007).

The quality of the hydrogen supplied to PEM fuel cells is critical due to the high sensitivity of the PEM system to impurities (Frost and Robinson 2007). For example, if gaseous H_2S (a constituent of methane – most common source of hydrogen) is exposed to the PEM assembly it can cause damage and degradation in reacting with the PEM and catalyst, which would lead to a reduction in efficiency and therefore performance of the fuel cell. It has been seen that a reduction of hydrogen permeation through a palladium membrane can be

reduced by a factor of 4 depending on the coverage of sulphur (Antoniazzi et al. 1989).

Therefore there is a need for high purity hydrogen to be delivered to maximize the potential and extend the lifetime of PEM fuel cell technology. This would improve its potential to be a viable alternative to fossil fuel combustion engines, not forgetting the durability and cost concerns that also need to be improved.

Current work on the membrane technology is aiming to:

- Reduce costs intrinsic material costs.
- Improve resistance of the membrane to impurities (CO and H_2S).
- Increase hydrogen permeability i.e. performance.

2.3 Gas Separation Mechanisms

There are a number of mechanisms that give time to the separation of gases using membranes; these include molecular sieving for porous membranes and surface diffusion or solution-diffusion for dense-metal membranes; more detail on these mechanisms can be found in Ockwig and Nenoff (2007).

The type of separation mechanism used depends on the type of pathway created by the membrane. Crystalline membranes commonly use surface diffusion or solid solution diffusion (Ockwig and Nenoff 2007). In amorphous materials, however, with their more random structure, the main mechanism used is solution-diffusion, but other mechanisms such as Knudsen diffusion are possible if pores are apparent in the membrane structure (Ockwig and Nenoff 2007).

These highly selective membranes only allow hydrogen atoms to diffuse through their structure and not any other gas, such as CO, CO_2, and N_2 etc (Ockwig and Nenoff 2007).

Ockwig and Nenoff (2007) describe the solution-diffusion mechanism in 7 steps illustrated in Fig. 2.

1. Adsorption: Firstly, the feed gas, consisting of hydrogen and impurities, is transported to the feed or retentate side of the membrane.

2. Dissociation: At the membrane surface the hydrogen is chemisorbed and dissociated into hydrogen ions (H^+) and electrons.

3. Ionisation: Hydrogen ions are then absorbed into the bulk membrane material.

4. Diffusion: Hydrogen ions and electrons then diffuse through the bulk material towards the permeate side of the membrane due to a difference in pressure created externally across the membrane.

5. Re-association: Hydrogen ions are then desorbed from the bulk material of the membrane to the permeate membrane surface.

6. Recombination: The ions and electrons then recombine or re-associate to form hydrogen molecules.

7. Desorption: Hydrogen molecules diffuse away from the permeate surface of the membrane.

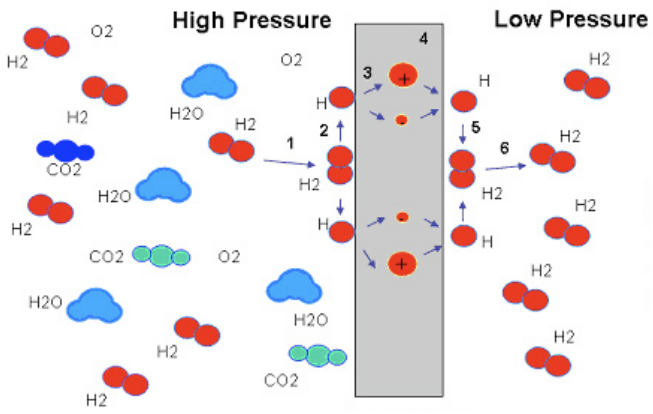

Fig. 2 Schematic of the solution-diffusion mechanism through a dense metallic membrane (www.sigma-tech.it)

The process is driven by a pressure difference between the retentate and permeate sides of the membrane i.e. by the hydrogen concentration gradient across the membrane in accordance with Fick's law. (Ockwig and Nenoff 2007, Adhikari and Fernando 2006, Sholl and Hao 2010).

$$J = -D\frac{\partial C}{\partial l} \qquad (10)$$

J is the diffusion flux, the amount of hydrogen per unit area per unit time.

D is the diffusion coefficient or diffusivity.

C is the concentration.

l is the length or width.

(Dolan, 2010)

The performance index 'flux', also known as permeation rate, is derived from this basic principle and can be used as a scaling factor to compare membrane performance (Adhikiri and Fernando 2006). Flux is defined as the total transport

of material through a membrane, (mol s^{-1} cm^{-2}). It can be combined with an expression for hydrogen permeance "flux per unit pressure difference between upstream (retenate) and downstream (permeate) sides" and then calculated using Sievert's Law.

Sievert's law predicts the solubility of gases in metal and typically predicts the solubility of hydrogen in crystalline metals where the hydrogen concentration is proportional to the square root of the hydrogen pressure, n = 0.5. However, in amorphous alloys this value can increase closer to 1 as hydrogen dissociation is limited on the surface of amorphous materials (Dolan 2010).

$$C = k\sqrt{P} \qquad (11)$$

C is the solubility

P is the partial pressure

K is Sievert's constant

As the calculation is based on the square root relationship (n=0.5) Dolan (2010) states "the flux of a given membrane varies with the difference in the square roots of the pressure at the high-pressure surface $P^{n}_{H.feed}$ and the low-pressure surface $P^{n}_{H.perm}$.

To calculate overall performance, Sieverts law and Ficks law are combined, equation (12).

“Equation – (Adhikari and Fernado 2006, Ockwig and Nenoff 2007)

$$N_{H_2} = \frac{\varnothing_{H_2}(P^n_{H.feed} - P^n_{H.perm})}{l} \qquad (12)$$

N_{H_2} is the hydrogen flux

$\varnothing_{H_2}$ is the hydrogen permeability

l is the membrane thickness

$P^n_{H.feed}$ and $P^n_{H.perm}$ are the hydrogen partial pressures in the retentate and permeate sides.”

In (12) ‘n’ is the assumed limit of dissociation, it is assumed to be 0.5 for Pd alloys and closer to 1 for Zr-based alloys, as they do not show the same catalytic activity for hydrogen dissociation. (Dolan et al. 2006, Dolan 2010). For permeance measurements a layer of Pd could be added to justify this assumption of n= 0.5.

Permeance can also be described as being inversely proportional to the membrane thickness (l) (Dolan 2010, Nenoff et al. 2006) highlighting the importance of utilizing a thin membrane to optimize performance while still considering the required mechanical properties, resulting in the process being limited by diffusion, discussed later.

Permeation rates, which depend on membrane thickness and temperature, are of critical importance in membrane performance as they allow for comparison when considering the diffusivity and solubility of the membrane. (Phair and Badwal 2006).

The diffusion coefficient's temperature dependence can be expressed using the Arrhenius equation (Adhikari and Fernando 2006).

$$\varnothing_{H_2} = K \exp\left(\frac{-E_{\varnothing}}{RT}\right) \qquad (13)$$

K is the pre-exponential factor constant (s^{-1}),

E is the activation energy (J/mol),

R is the gas constant ($J\ K^{-1}\ mol^{-1}$),

T is the absolute temperature (K).

This enables a method for permeability to be calculated and so compared across different membrane compositions.

Additional parameters to those of membrane composition, structure and hydrogen concentration also hold great significance to membrane performance or 'flux'. Two factors related to membrane flux have been identified in order to quantify performance and determine the optimal in-situ conditions for optimizing output.

1. Firstly a flux-thickness relationship is intuitive considering the previously mentioned critical thickness value. Dolan et al. (2006), Phair and Badwal (2006) and Dolan (2010) all note the significance of thin membranes (< 20 microns) being useful to eliminate the diffusion-limiting aspect and so transfer the attention to trying to optimize the dissociation-limiting factor to optimize performance.

2. Secondly a flux-pressure relationship has been derived (Ockwig and Nenoff 2007, Hara et al. 2002, Phair and Badwal 2006). The pressure difference between the retentate and permeate side controls the pressure gradient across the membrane. This is an important factor that contributes to determining the rate of diffusion and solubility, and therefore the hydrogen flux, of the membrane. Too high pressure and the membrane structure may fail due to the high pressure on the thin membrane structure; too low pressure and the pressure gradient will not be sufficient to promote diffusion across the membrane.

2.4. Membrane General Principles

Non-Pd-based crystalline and amorphous dense-metal membranes for hydrogen purification all commonly require a thin layer < 500 nm of Pd (Dolan et al. 2009, Chin et al. 2011) to promote hydrogen dissociation and protect against surface oxidation of the underlying membrane materials. (Horikawa et al. 2010, Hara et al. 2002, Sholl and Hao 2010). This allows the base alloy membrane to reduce the

potential for the permeability to be dissociation-limited, as only a thin layer of expensive Pd is needed.

Materials which exhibit high hydrogen permeability desirable for a membrane application, such as rapid diffusion of hydrogen through membranes, are found in transition metals which form BCC crystal structures, i.e. Ti, Zr, V, Ta, Nb (Dolan et al. 2010). Transition metals are of great interest for membrane alloys, as they exhibit high values of hydrogen solubility and/or diffusivity (Dolan et al. 2009, Dolan 2010), which result in high values of hydrogen permeation (Paglieri et al. 2006). The production of these membranes come with a number of compositional and technological barriers such as reducing the mechanical/structural degradation, *i.e.* hydrogen embrittlement at higher temperatures (above 500 °C), including in-cycling, and surface poisoning to produce hydrides that are not brittle, before the use of such membrane materials can be considered (Ockwig and Nenoff 2007, Dolan et al. 2010).

2.4.1 Crystalline Membranes

The attraction of pure crystalline Pd membranes comes from their infinite selectivity for hydrogen (Tong et al. 2004) but they can only operate at high temperatures. Below 300 °C Pd shows a regime where the alpha (α) and beta (β) phases coexist during hydrogen absorption. The critical point for the β-phase above which it cannot form is 295 °C and 21 bar. As the two phases hold significantly different lattice constants at lower temperatures there can be significant internal stress created by 10% lattice expansion (Knapton 1977). This

promotes cracking or hydrogen embrittlement of the membrane when temperature cycling between the two phases (Wicke and Nernst 2010).

Palladium is also very expensive, and according to (Dolan 2010), even a 5-micron thick pure Pd membrane equates to a cost that exceeds the targeted cost for hydrogen separation membranes set out by the DOE for 2015 (DOE Monthly Review 2013). This highlights cost as a major barrier in expanding this technology, especially for use in providing pure hydrogen for smaller, mass producible applications such as PEM fuel cells.

Pd-alloy membranes are also highly sensitive to gaseous impurities such as sulphur, CO and H_2S, which cause surface contamination (Ockwig and Nenoff 2007). This dramatically reduces membrane performance due to the membrane surface no longer being defect-free, reducing the available membrane surface area for adsorption of hydrogen (Antoniazzi et al. 1989, Ockwig and Nenoff 2007) and can lead to high porosity, poor selectivity (Wei and Brewer 1996) and/or complete failure (Dolan et al. 2006, Hara et al. 2000).

Primarily silver (Ag) has been used to alloy with Pd to minimize the membrane cost, susceptibility to impurities and embrittlement effect (Dolan 2010, Ockwig and Nenoff 2007). The use of Ag is to avoid hydrogen embrittlement by avoiding the alpha to beta phase transition, improving the permeability by increasing the solubility. This is achieved by lowering the hydrogen absorption enthalpy (Donlan et al. 2006) so that the critical pressure and temperature are lowered as well as lowering the activation energy of the membrane, potentially by over half,

through the increasing the mol fraction of Ag from pure Pd to $Pd_{0.5}Ag_{0.5}$ (Holleck 1969, Van Delft at al. 2006). Although less expensive than pure Pd membranes, it is still, however, an expensive membrane composition.

Crystalline palladium-silver alloy (Pd-Ag) membranes are, however, presently the industrial standard in terms of membrane hydrogen separation (Dolan 2010). The specific lattice structure of palladium, including its high rate of diffusion due to the solution-diffusion mechanism (Kikuchi 1995), ability to take in "large quantities of hydrogen" into solution and resist significant lattice expansion above 300 °C during hydrogen absorption (Knapton 1977), allow only hydrogen and no other substance or impurity to pass through, are all significant factors in its industrial use. These properties result in providing near perfect selectivity of hydrogen and producing purities up to 99.9999% (Kikuchi 1995).

Aiming at finding more cost effective membranes, a number of alternative membrane compositions have been investigated. For example Ni- with either Nb (Dolan et al. 2009, Sholl and Hao 2010, Chin et al 2011), Zr (Hara et al. 2002, Jayalakshmi et al 2010, Ockwig and Nenoff 2007) or P (Dos Santos and Miranda 1997), have been investigated to try to find a robust and cost effective solution to providing high purity hydrogen, with permeability rates approaching or comparable to those of Pd and/or Pd-Ag (Dolan et al. 2009, Horikawa et al. 2010, Hara et al. 2010, Sholl and Hao 2010, Chin et al. 2011, Dolan et al. 2011, Jayalakshmi et al. 2010, Peachey et al. 1996, Shimpo et al. 2006).

One crystalline non-palladium membrane alternative has been found to exhibit permeability values that exceed some Pd-based membranes at 400 °C (Chin et al. 2011). These membranes have a similar composition to the previously mentioned Ni-Nb-Zr-Ta amorphous alloy (Chin et al. 2007) with the composition $Ni_{42}Nb_{28}Zr_{25}Ta_5$ (at%). However, all the crystalline membranes failed during the permeation tests due to severe hydrogen embrittlement when temperature either increased or decreased from their start temperatures ranging between 300 °C and 450 °C (Jayalakshmi et al. 2010).

Amorphous membranes of similar composition in this study, however, did not fail, highlighting a trait that amorphous alloys inherently guard against. The amorphous membranes, however, exhibited the permeability values an order of magnitude lower than the crystalline membranes of the same composition in this study (Jayalakshmi et al. 2010).

Dolan et al. (2011) find another bcc based membrane composition $V_{85}Ni_{10}M_5$ (where M represented either Si, Mn, Fe, Co, Ni, Cu, Pd Ag, or Al) which was found to have a hydrogen permeability of 9.3 x 10^{-8} mol m^{-1} s^{-1} $Pa^{-0.5}$ at 400 °C; a value comparable to the bench mark of Pd membranes of approximately 10^{-8} mol m^{-1} s^{-1} $Pa^{-0.5}$ at 327 °C (Yamaura et al. 2005). Control of the solubility in the membrane so that hydrogen embrittlement is prevented, but still allowing the naturally high permeation values to be exhibited, was tested with the varying percentages (5 – 31.5 %) of each metallic element in the base composition (Co, Ni, Fe, Mn, Pd, Ag, Al). Control was carried out by undertaking all solubility experiments at 400 °C and up to 12 bar.

The balance of alloying composition requires extreme precision, shown as increasing the Zr content by only a few percent proved to show a trend of increasing permeability with an increasing Ni/Zr ratio (Dolan et al. 2009). The phase concentration of both Ni and Zr, consequently, increased with the trend, lowering the Nb phase therefore reducing the membrane's ability to resist crystallization, hence increasing risk of hydrogen embrittlement. Furthermore, the effects of differing ratios of Ti and Ni were studied by Tang et al. (2008) and Hara et al. (2002). In Tang et al. (2008), $Nb_{40}Ti_xZr_{12}Ni_{48-x}$ composition variations were used, where Ti increased permeability and ductility and Ni substitutions increased permeability further but caused a reduction in ductility.

Therefore, there are research projects (Sakamoto et al 1984, Strom-Olsen et al. 1991, Dolan et al. 2009, Tang et al. 2008, Hara et al. 2002, Sholl and Hao 2010, Sholl and Hao 2011, Chin et al. 2011, Dolan et al. 2011, Jayalakshmi et al. 2010, Wang et al. 2013) that have aimed, and are continuing to aim, to find a more cost effective membrane, either by drastically reducing the amount of Pd used or by finding a non-Pd based option, which has permeability values that are comparable to Pd crystalline membranes but operate at lower temperatures.

One promising alternative is the use of amorphous alloys.

2.4.2 Amorphous Alloy Membranes

Current literature (Dos Santos and Miranda 1997, Dolan et al. 2009, Horikawa et al 2010, Hara et al. 2002, Sholl and Hao 2010, Sholl and Hao 2011, Jayalakshmi et

al. 2010, Hao et al. 2009, Hao and Sholl 2008, Shimpo et al 2006) demonstrates the continuing research into, and interest in, amorphous metallic membranes. Most are aimed at developing a membrane that exhibits performance approaching the present best-performing Pd/Pd-Ag based membranes but at a reduced material cost and with comparable hydrogen permeation and diffusivity. The advantages and disadvantages are discussed here.

Amorphous alloy structures have two main advantages over crystalline counterparts:

1. They possess an open and non-uniform crystal structure. This means there is no need to achieve a defect-free surface (Ockwig and Nenoff 2007) required by crystalline membranes to avoid hydrogen trapping. Defects, like dislocations, in amorphous membranes facilitate the diffusion and solubility for hydrogen in their crystal structure to aid diffusion at lower temperatures (Ockwig and Nenoff 2007) with a lower risk of hydrogen embrittlement by providing space and differing energy binding sites. The same defects in crystalline membranes tend to cause hydrogen traps (Ockwig and Nenoff 2007) due the specific binding energies exhibited by the bulk of the structure, causing internal stress on the membrane that can lead to hydrogen embrittlement and failure.

2. Amorphous alloys exhibit augmented mechanical and structural properties such as increased ductility, corrosion resistance, improved strength and superior hydrogen solubility compared to their “crystalline analogues” (Ockwig and Nenoff 2007) by nature of their atom arrangement. The improved mechanical

properties of amorphous alloys may prove superior to crystalline counterparts as they have the potential to allow for a reduction in membrane thickness without hindering mechanical performance.

The physical structures of amorphous alloys and crystalline membranes have significant effects on the diffusivity of hydrogen through the membrane (Dos Santos and Miranda 1997). The advantages and disadvantages are reviewed here.

Amorphous alloys, due to being fabricated by rapid solidification, form with high defect content. This formation increases the solubility of the material to hydrogen (Dos Santos and Miranda 1997) but conversely initially inhibits the diffusivity of the material as more hydrogen is chemically bonded to the host material in the numerous and often deep defects (Sakamoto et al. 1984).

When hydrogen is adsorbed into the bulk material it is initially preferentially attracted to high energy binding sites, which act as hydrogen traps, therefore restricting the atom's mobility. Defects and dislocations act as these high energy-binding sites and slow hydrogen permeation.

However, as hydrogen concentration increases in the bulk material of the membrane, and all high energy binding sites are occupied, hydrogen atoms populate lower energy binding sites (Dos Santos and Miranda 1997). This increases the hydrogen mobility within the structure and so increases hydrogen flux and permeability "due to the structural disorder of these amorphous metals" (Dos Santos and Miranda 1997).

Therefore diffusion is said to be "hydrogen concentration dependent" (Sakamoto et al. 1984, Strom-Olsen et al 1991, Dos Santos and Miranda 1997, Sholl and Hao 2010, Sholl and Hao 2011, Hao and Sholl 2008), in these randomly ordered materials, which explains why the same concentration dependence is not seen in highly structured crystalline metals (Dos Santos and Miranda 1997).

The disadvantages of crystallization of these amorphous alloy membranes include reduced hydrogen permeation due to fewer varied energy binding sites being available and a reduction in mechanical strength due to increased medium range and long rang ordering, allowing trapped hydrogen to cause larger internal stresses on the crystal structure leading to induced hydrogen embrittlement.

Much of the focus for amorphous alloy membranes is on Early Transition Metals (ETM) as they have been identified by Paglieri et al. (2006), Dolan et al. (2009) and Dolan (2010) to show the most promise in demonstrating hydrogen permeabilities, including the diffusivities and flux rates similar to crystalline Pd-Ag alloys.

2.4.2.1 Early Transition Metals: Diffusion and Hydrogen Concentration

Early transition metals (ETMs) are known to exhibit high hydrogen permeabilities (Dolan et al. 2009). Ni-based constructions are a popular base of research and have been alloyed with a number of other elements such as Zr, P

and Nb with an aim of maximizing permeability values (Strom-Olsen et al. 1991, Dos Santos and Miranda 1997, Dolan et al. 2009, Horikawa et al. 2010, Tang et al. 2008, Hara et al. 2002, Sholl and Hao 2010, Chin et al. 2011, Dolan et al. 2011, Jayalakshmi et al. 2010, Shimp et al. 2006). The aim is to prevent hydrogen embrittlement and/or increase the operating temperature, (in an ideal world to above 700 °C for membrane reactors) by increasing crystallization temperature.

An early study (1991) by Strom-Olsen et al. experimented with the diffusion of hydrogen in the metallic glass Ni_{60}-Zr_{40} in investigating its hydrogen binding and diffusion behaviour. The authors utilized permeation-loading studies to determine the binding energy of hydrogen to the host metal and the number of binding sites available for this to occur.

More recent investigations into diffusion characteristics found that due to hydrogen diffusion through crystalline metallic materials being limited by the specific binding sites available and diffusion paths in its long-range order, diffusivity is said not to be concentration dependent (Hao and Sholl 2008). The varied energy binding sites available throughout the material, however, define amorphous materials diffusivity; therefore hydrogen concentration has been shown to only significantly affect the diffusion rates of amorphous or glassy metals (Sakamoto et al. 1984, Strom-Olsen et al. 1991, Dos Santos and Miranda 1997, Sholl and Hao 2010, Sholl and Hao 2011, Hao and Sholl 2008).

Sakamoto et al. (1984) agrees with Strom-Olsen et al. (1991), (among others; Dos Santos and Miranda 1997, Sholl and Hao 2010, Sholl and Hao 2011 and Hao

and Sholl 2008) in identifying the different structural characteristics leading to differing diffusion behaviour, and so suggest that Sievert's law, which determines diffusion rates, or hydrogen concentration, and therefore flux in crystalline metals, does not apply to amorphous materials for any concentration.

This behaviour can also not be described by the original definition of Ficks law due to its need for one fixed path or set binding energies. Therefore, the assumption of differing binding site energies is needed so that when combined with Sievert's law, the hydrogen permeance behaviour can be applied to amorphous materials, i.e. equations (10-12).

The adjustment to Sievert's law, therefore, allows currently emerging and developing amorphous alloy performance to be quantified and then compared to similar composition crystalline alternatives and commercial Pd-Ag membranes. Especially useful to compare to Pd based membranes currently used in industry, which are the benchmark, roughly 10^{-8} (mol m^{-1} s^{-1} $Pa^{-0.5}$) at 350 °C (Yamaura et al. 2005) for membrane performance.

Dos Santos and Miranda (1997) presents a comparison of diffusivity and solubility in both amorphous and crystalline alloys. Notably the solubility of hydrogen in amorphous alloys was significantly higher than in crystalline counterparts. This is in line with Strom-Olsen et al. (1991)'s findings and again identifies the multi-defect nature of amorphous alloys to potentially be advantageous in hydrogen transport applications.

The results further develop the hydrogen flux-concentration relationship by describing the mechanism of hydrogen diffusing into the host lattice i.e. its solubility; also termed 'hydrogen trapping' (Sakamoto et al 1984, Jayalakshmi et al 2010). As hydrogen concentration increases, the higher energy micro-void binding sites are filled causing hydrogen to bind to lower energy binding sites. As hydrogen concentration increases, with increasing pressure, the influence of high-energy binding sites on hydrogen mobility is therefore reduced (Dos Santos and Miranda 1997). Therefore flux and diffusion of hydrogen through the metal is increased, showing the dependence of flux on hydrogen concentration (Sakamoto et al 1984, Strom-Olsen et al. 1991, Dos Santos and Miranda 1997, Sholl and Hao 2010 and 2011, Hao and Sholl 2008).

2.4.2.3 Membrane Limitations

Membrane permeation is commonly known to be either diffusion- or dissociation-limited (Dolan et al. 2006, Ockwig and Nenoff 2007).

The deciding factor in determining which mechanism limits the rate of permeation is the membrane critical thickness. This is a thickness value above which the process is limited by bulk diffusion and below which is limited by the ability of the membranes retentate side to dissociate hydrogen (Dolan et al. 2006).

As the investigation to be undertaken in this report considers a melt spun amorphous membrane, where typical thicknesses of 30-50 microns (Dolan et al. 2006) are produced by such a technique, the limiting factor will tend to be

dissociation-limited because the thickness of membranes in this study are typically less than 30 microns. This is because any further reduction in thickness cannot increase permeability via faster diffusion as the dissociation of hydrogen has already reached its maximum. Although if desired, a Pd-alloy catalyst layer can be sputtered onto the membrane surface to improve the dissociation reaction. (Dolan et al. 2006, Ockwig and Nenoff 2007, Van Delft et al. 2006, Holleck 1969).

Pd alloys have been shown to have infinite selectivity (Tong et al. 2004), which is constantly trying to be recreated in so called "non-Pd" membranes to cut costs. However, Dolan et al. (2006) note that even some "non-Pd" membranes use a sputtered layer of Pd on their surface to prevent oxidation, sometimes to provide sulphur tolerance and also to aid in the dissociation process. Furthermore, crystalline Pd has been shown to promote dissociative action compared to alternative materials such as Ni (Hara et al. 2002), lowering the activation energy barrier.

It is therefore noted by many studies (Dolan et al. 2006, Phair and Badwal 2006, Dolan et al. 2011, Shimpo et al. 2006) that Pd is still an essential component of all membrane structures, especially for improving dissociation. Although using Pd increases material costs significantly compared to other metals, the large reduction in mass compared to Pd-Ag membranes, from the order of microns to sometimes less than 150 nm (Chin et al. 2011) means a substantial reduction in cost.

2.4.3 Hydrogen Solubility

During the separation process through a Hydrogen Separation Membrane (HSM) the number of hydrogen atoms (H) to host metallic atoms (M) can be expressed as a ratio to give an indication of hydrogen solubility within the membrane. This method allows a performance comparison of membranes whether fully amorphous, fully crystalline or comprising of more than one phase, using the Hydrogen/Metal (H/M) atom ratio (Sholl and Hao 2010).

As hydrogen flux is dependent on hydrogen concentration gradient for amorphous alloys and hydrogen's ability to move through the membrane, an increase in the H/M ratio typically will result in an increase in hydrogen solubility within the host lattice. Therefore, a high H/M value is preferred to increase membrane performance due to the premise of filling binding sites with different bonding energies via solution-diffusion allowing the low binding energy sites to release hydrogen more readily (Strom-Olsen et al. 1991, Sholl and Hao 2010, Hao et al. 2009, Hao and Sholl 2008, Ockwig and Nenoff 2007).

Furthermore, the action of hydrogen permeation into the host material slightly expands the metallic lattice, further aiding the creation of more free volume for hydrogen transport (Dos Santos and Miranda 1997, Ockwig and Nenoff 2007).

2.4.4 Alloying

Along with the addition of Pd coatings there is a general consensus (Strom-Olsen et al 1991, Dolan et al. 2006, Horikawa et al. 2010, Tang et al. 2008, Hara et al. 2002, Sholl and Hao 2010 and 2011, Chin et al. 2011, Jayalakshmi et al. 2010, Shimpo et al. 2006, Ockwig and Nenoff 2007) that alloying of the base material is needed to maximize the physical properties of the membrane while maintaining the random amorphous structure needed for H_2 permeation (Ockwig and Nenoff 2007). The addition of different alloying components to amorphous alloys in differing compositions has been widely reported in the references above but one is yet to equal or better the performance of Pd based membranes in all areas (temperature range, diffusivity, solubility, dissociation etc).

This is the target of all ongoing research and it depends heavily on the specific material composition.

Adhikari and Fernando (2006), Sholl and Hao (2011), Dolan et al (2011) and Shimpo et al. (2006) all report that alloying of the base material membrane leads to improved properties with a number of studies using Ni as the foundation material and alloying using either Zr (Strom-Olsen et al. 1991, Horikawa et al. 2010, Tang et al. 2008, Hara et al. 2002, Sholl and Hao 2010, Jayalakshmi et al. 2010, Ockwig and Nenoff 2007), P (Dos Santos and Miranda 1997) or Nb (Dolan et al. 2009, Sholl and Hao 2010, Chin et al. 2011, Jayalakshmi et al. 2010).

2.4.4.1 Zirconium

Jayalakshmi et al. (2010) 's study on the hydrogenation properties of Ni-Nb-Zr-Ta amorphous ribbons found that increasing Zr content, from 20 to 25 at%, decreased the crystallization temperature of the amorphous alloy, showing the dependency of thermal properties on composition. This is echoed by Dolan et al. (2009)'s findings on Ni-based membranes at 400 °C where crystallization temperature differed by 60 °C due to changes in composition; $Ni_{60}Nb_{10}Zr_{30}$ (579 °C) to $Ni_{60}Nb_{40}$ (640 °C).

However, adding Zr led to increased hydrogenation kinetics, i.e. a reduction in the crystallisation temperature, permeability values increased to 2.1 x 10^{-9} $mol.m^{-1}.s^{-1}.Pa^{-0.5}$ ($Ni_{64}Zr_{36}$) from 1.6 x 10^{-9} $mol.m^{-1}.s^{-1}.Pa^{-0.5}$,($Ni_{60}Nb_{20}Zr_{20}$) at 350 °C and lowered activation energy for desorption from 28 ± 1 $kJ.mol^{-1}$ to 21 ± 1 $kJ.mol^{-1}$ for $Ni_{64}Zr_{36}$ and $Ni_{60}Nb_{20}Zr_{20}$, respectively. Furthermore, the low-Zr variation exhibited superior strength in uniaxial loading and Hara et al. (2002)'s review on amorphous alloys membranes notes that Zr, along with Ni and Cu base materials, have the highest reported glass transition (T_g) values, showing it cannot be discarded altogether to further increase crystallization temperature.

2.4.4.2 Niobium

Increasing Nb content in a Ni-based membrane enabled it to increase its crystallization temperature according to Dolan et al. (2009). Their experiment used DSC to identify the crystallization behaviour and showed an increase of

resistance to crystallization with an increasing Nb:Zr ratio over 100 °C. It was also found that a Ni-Nb composition including Ta showed, comparatively, the greatest resistance to crystallization of any tested (Dolan et al. 2009).

2.4.4.3 Titanium and Nickel

Hara et al. (2002) similarly substituted Ti and Hf into a Pd-coated Zr-M-Ni amorphous alloy membrane. Using a similar temperature range to Tang et al. (2008) (200 – 350 °C), the permeation of the varying membrane compositions decreased with the addition of both Ti and Hf due to an increase in the activation energy of permeation. However, an increased Hf content produced a similar effect to that of reducing Zr content by increasing the crystallization temperature, and so stabilizing the phase.

2.4.4.4 Disadvantages of Alloying

Sholl and Hao (2011), computationally predicting Zr-Cu-Al alloy performance, note the other possible disadvantages of alloying with Al. Specifically alloying the original composition of $Zr_{54}Cu_{46}$ to form $Zr_{45}Cu_{45}Al_{10}$, which significantly decreased the permeability of the membrane by 2 orders of magnitude.

Pd alloy membrane permeability values were exceeded by half an order of magnitude with increasing test temperature by Shimpo et al. (2006) testing an Ni-Nb-Zr-Co composition. Operation at 300 °C proved to be successful, even for long term (100 h) testing. However, testing of the same amorphous membrane

with a Pd coating to improve dissociation at 400 °C highlighted the issue of higher temperature operation with amorphous alloys as the permeability of the membrane significantly decreased with time, attributed to diffusion of Pd into the amorphous membrane matrix.

2.4.5 Temperature

Operation temperature of the membrane application is of critical importance. The change in operating temperature will have a significant effect on the membrane solubility and therefore performance.

Amorphous alloys are well documented in having a crystallization point in the region below 300-400°C (Ockwig and Nenoff 2007, Dolan et al. 2006 and 2009, Dolan 2010).

This presents two options:

1 – Use lower temperature ranges i.e. below 400 °C, which may be lower than the required industrial standard for such applications as membrane reactors (Dolan et al. 2006 and 2009, Ockwig and Nenoff 2007) but could be potentially used as hydrogen purification methods for lower temperature systems such as hydrogen production for PEM fuel cells and aim to improve flux at these temperatures.

Or

2 – Increase the crystallization temperature of the membrane by the careful addition of alloying elements, such as Zr (Strom-Olsen et al. 1991) or Nb (Dolan et al. 2009). However, this comes with the issues highlighted in the previous section that depend on the membrane composition. This may not be a straightforward and totally accomplishable task as the result may not increase the crystallization temperature and also may reduce other properties such as permeability (Sholl and Hao 2011).

2.4.6 Conclusions

Recent work may have advanced the methods for identifying a potential comparable membrane composition to the existing Pd-based benchmark. Sholl and Hao (2011) use a mathematical model of combining first principles density functional theory calculations and statistical mechanics, which uses no experimental data in its procedure, and compares the initial predictions to known experimental findings to determine its accuracy.

The theoretical model enables a quick search for potential membrane materials, which can then be investigated experimentally, including ZrCu and ZrCuTi systems (Sholl and Hao 2011).

2.5. Aims of the Project

Two systems, ZrCu and ZrCuTi, were identified by Sholl et al. (2011) using a theoretical first principles model, as having compositional regions that could have promising permeabilities similar to Pd. Further simulations including Hao and Sholl (2008) also show that the specific binary alloy (ZrCu) may hold promise in solubilities and permeabilities comparable to Pd/Pd-Ag membranes. As a starting point in investigating these the ZrCu and ZrCuTi systems, this study has chosen $Zr_{45}Cu_{55}$ and $Zr_{22}Cu_{64}Ti_{14}$ as target compositions.

The study aims to investigate the thermal characteristics and behaviour under hydrogen of these compositions, to enable a clearer idea of their use as separation membranes. Fig. 3 below shows the Zr-Cu phase diagram, which demonstrates a number of different possible phases, if the alloys are allowed to cool at an equilibrium rate. For the $Zr_{45}Cu_{55}$ target composition (equivalent to Zr54Cu46 in wt%), the phase diagram indicates that the CuZr and $Cu_{10}Zr_7$ phases would form when the liquid was cooled to 916 °C, followed by the possible formation of Cu_5Zr_8 (730 to 712 °C) and alpha $CuZr_2$ (712 °C). However, such phase diagrams only show phases that are expected to form under equilibrium conditions, whereas the cooling rate during melt spinning (of the order of the order of 10^4–10^7 °C/s (Cahn 1983)) is certainly non-equilibrium.

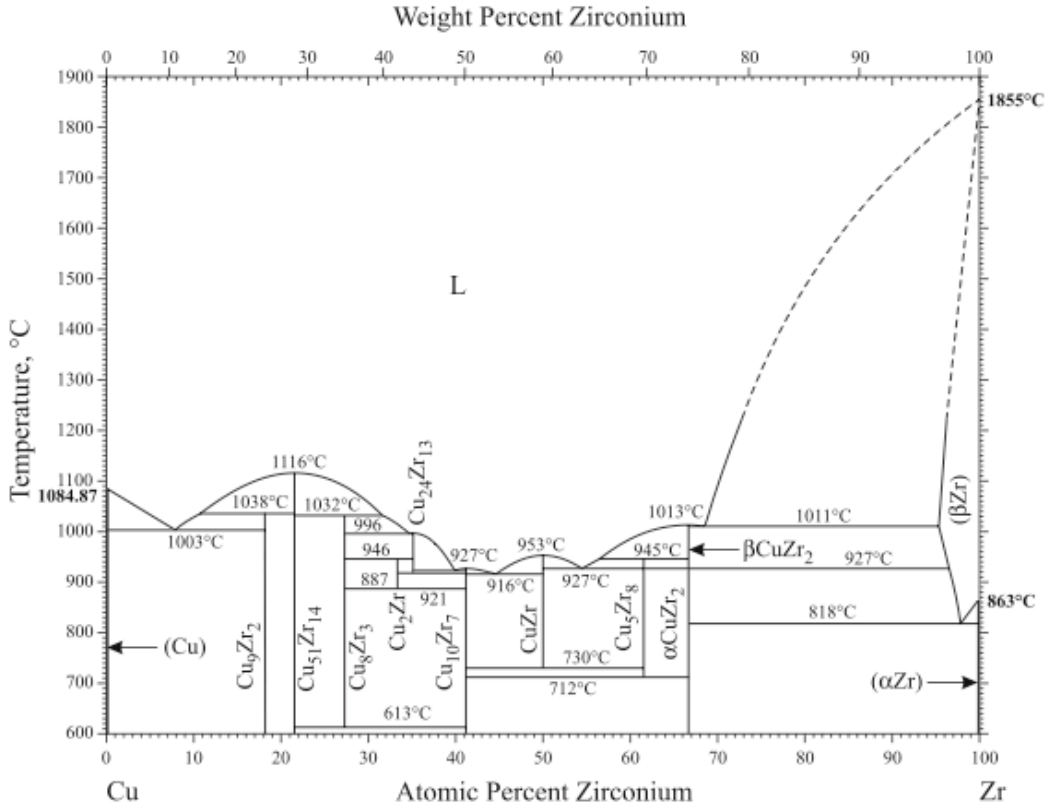

Fig. 3 Zirconium-Copper phase diagram (Okamoto, 2008)

The experimental aims are as follows:

- Fabricate samples of amorphous Zr54Cu46 and Zr30Cu60Ti10 (wt%) materials by rapid solidification using a melt spinning technique.
  (This is $Zr_{45}Cu_{55}$ and $Zr_{22}Cu_{64}Ti_{14}$ in at%)
- Characterize the microstructures and thermal behaviour of the amorphous Zr-Cu-based melt-spun ribbon samples by XRD and DSC (Ar and H_2).
- Determine the hydrogen permeabilities of the ribbons using a membrane test rig, and the hydrogen solubilities using an IGA.

3. Experimental Methods

3.1. Alloy Material Manufacture by Arc Melting

Zr (99.98% purity from Advent Research Materials) and Cu (99.999% purity from Goodfellows) plate were weighed (3 dcp) to produce 10 g of the $Zr_{45}Cu_{55}$ (Zr54Cu46 wt%) target composition. The charge was loaded on to a water-cooled copper hearth within the arc furnace. Once pumped down under argon an electrical current produces an arc that strikes a titanium getter, in order to remove any remaining oxygen in the chamber. The arc is then applied to the charge to produce a molten state to couple the materials. The sample is melted several times to ensure homogeneity and then cooled to form a button. The button is mechanically cut with a saw into 0.8 mm diameter sample to fit the melt spinner crucible. This method is easily repeatable for different compositions as well as adding Ti (99.9999% purity) to produce the $Zr_{22}Cu_{64}Ti_{14}$ (Zr30Cu60Ti10 wt%) target composition.

3.2 Membrane Manufacture by Melt Spinning

3.2.1 Melt Spinning

Hydrogen permeation membranes have been successfully manufactured using melt spinning (Dos Santos and Miranda 1997, Dolan et al. 2006, Hara et al. 2002,

Dolan 2010, Jayalakshmi et al. 2010) which produces amorphous ribbons of thicknesses 30-70 microns.

As mentioned previously a significant factor in membrane performance involves the membrane thickness. In trying to reduce the number of available limiting factors that could reduce membrane performance, a thin membrane (< 30 microns) enables the diffusion-rate as the limiting factor to be discarded (Dolan et al. 2006) and so leads to potentially only a dissociation-rate limited feature.

If permeation rates are insufficient, then as an alternative, the addition of a Pd coating has shown to improve dissociation rates by an order of magnitude and so increase performance (Ockwig and Nenoff 2007). On a membrane this thin and small even a thin film (a few microns) of Pd deposited on to the membrane by sputtering (Yamaura et al. 2004) will not increase the cost significantly compared to Pd membranes.

An Edmund Buhler GmBH Melt Spinner SC was used to fabricate the amorphous alloy membranes. The standard manufacturing method is as follows:

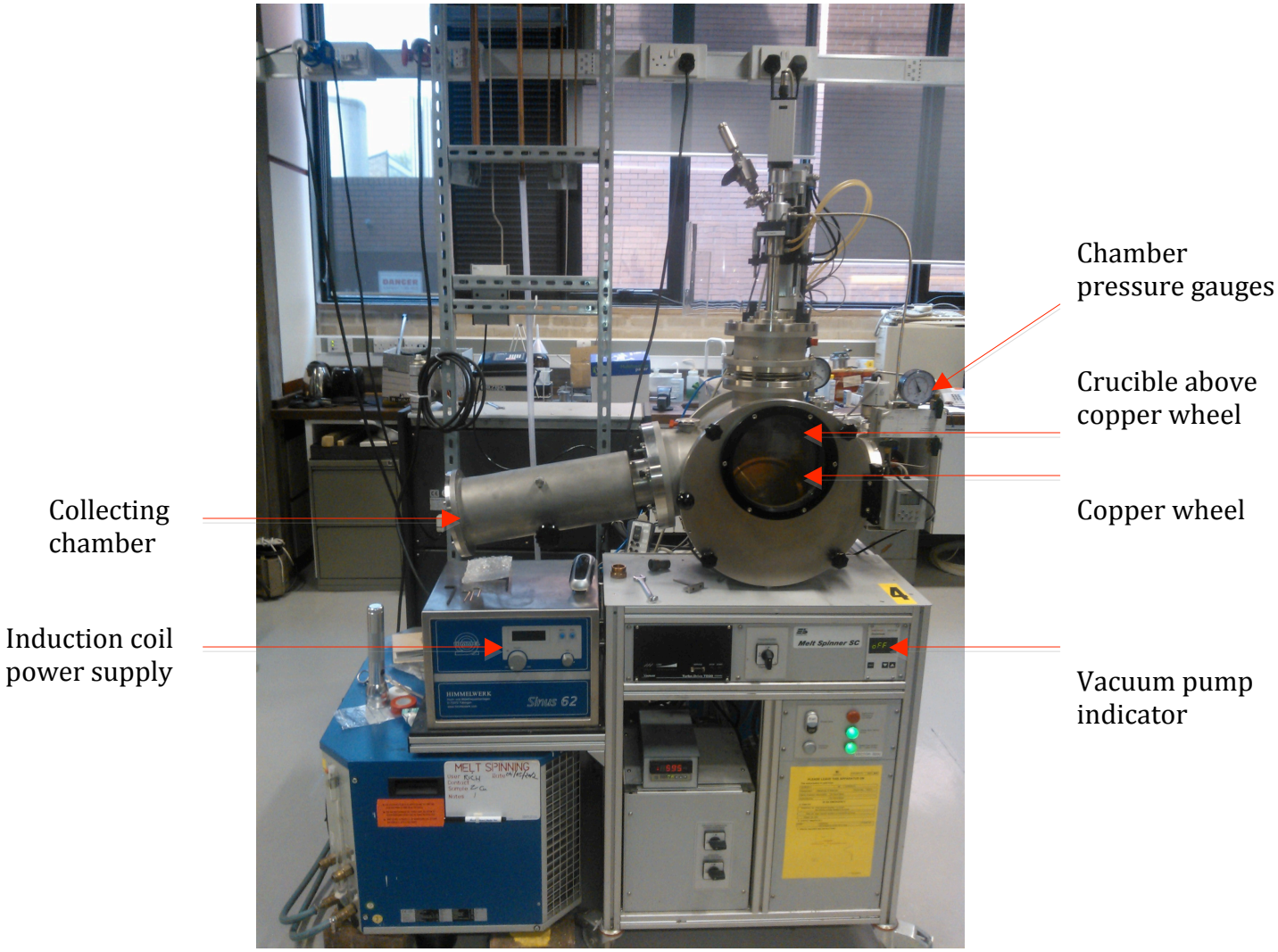

Fig. 4 Photograph of the Edmund Buhler GmBH Melt Spinner SC

The alloy sample is loaded into the crucible under argon in a glovebox. The sample and crucible are then removed and positioned above a copper wheel in the melt spinner. This is only achievable under air but the chamber encasing the crucible and wheel is evacuated as soon as possible, ensuring an ejection gap

distance between wheel and crucible of 0.3 cm. Three cycles of filling with argon and evacuating to 10^{-3} mbar ensure minimum exposure to air once the sample is loaded. The chamber is then exposed to a vacuum of 10^{-6} mbar (the maximum capability of the vacuum) before the operation cycle begins. Once the wheel is spinning at 50 Hz the induction coil around the crucible heats the sample above the melt point for the specific alloy (925 °C for $Zr_{45}Cu_{55}$). The parameters chosen are due to standard practices to produce amorphous materials. Temperature is measured using an integrated pyrometer. The sample is then ejected onto a rotating copper wheel (50 Hz), which rapidly cools the sample (up to 10^7 ˚C/sec (Strom-Olsen et al. 1991) to form a solid amorphous ribbon. The ribbon is then collected in the neighbouring chamber.

3.3 Scanning Electron Microscope (SEM)

A JEOL 6060LV microscope was used to observe the microstructure of each sample. Secondary Electron Imaging (SEI) and Back Scattered Electron Imaging (BEI) were used to identify amorphous and crystalline regions as well as pores and general ribbon structure. Energy Dispersive Spectroscopy (EDS) was used in conjunction with Oxford Instruments INCA EDAZ software to collect composition data, which was averaged out over the ribbon.

Samples were prepared by mounting on an aluminium base using carbon stickers. Surface imaging was undertaken to identify the microstructure and composition immediately after melt spinning.

3.4 Thickness Measurement

The thickness of each of the ribbons was measured using a micrometer to identify permeability potential and compare to the literature. Measurements were taken over a number of sections of ribbon, aiming at sections at the start, middle and end of the ribbon. Due to the random nature of picking ribbon to measure, it was assumed a good variety of ribbon from the start and end of the process was chosen. Also at each section, thickness measurements were recorded across the width if possible (some ribbons were only a few millimeters wide).

3.5 Powder Preparation

Ribbons were milled into fine powder for use in the DSC, IGA and for XRD measurements using a Spec Certiprep 6750 Freezer/Mill. The sample was loaded inertly into the polycarbonate crucible along with the steel milling bar. Once loaded into the freezer-mill the bath was filled with liquid nitrogen and the sample were submerged. After 30 minutes the freezer-mill was set to run 3 cycles of 1 minute milling time with 3 minutes cooling in between so as not to induce any heat induced crystallization of the sample. The freezer mill uses electrical current put through two coils over each end of the crucible to produce an electromagnetic field forcing the milling bar back and forth, milling the ribbon. The process was repeated at least 8 times to ensure a fine powder was produced.

3.6 Thermal Analysis

Thermal analysis of each sample was undertaken using a Netzsch DSC204HP Differential Scanning Calorimeter (DSC) placed in an argon glove box. Samples were measured under both hydrogen and argon atmospheres. The full heating range was utilized from 30 to 500 °C for most hydrogen heating profiles with a heating rate 2 °C/min. Each sample was heated and then left to cool to room temperature before performing the second heating profile. Pressurized measurements were conducted at 3 bar at a flow rate of 100 ml/min.

3.7 Determination of Hydrogen Sorption Characteristics

A constant-pressure TGA (Hiden Analytical IGA) was used to measure the hydrogen sorption characteristics of a sample in terms of weight gain and loss. The system can measure mass, temperature and pressure against time. This is achieved by detecting deflections on a bottom-loading balance as a voltage, which is attached to a galvanometer so the voltage can be converted into a mass. Typically 100 mg samples are used, temperature range -196 °C (if cryo-chamber attached) to 500 °C, with a pressure range of 1 – 20 bar. The IGA has a long-term stability of ±1 μg and a weighing resolution of 0.2 μg.

The samples were inertly loaded and cycled in argon up to 100 times between 1050 and 1250 mbar at room temperature so to try to minimize exposure to air. Absorption measurements were performed at 1 and 3 bar. The heating profile

ran from room temperature to 400 °C at 2 °C/min. It can be run for isotherms or isobar measurements.

3.8 Crystal Structure Determination

A Bruker D8 X-ray Diffraction (XRD) advance spectrometer was used to determine the crystal structure of powdered samples. Powder x-ray diffraction was undertaken using CuKα radiation and a Göbel mirror, Kα (λ = 1.5406 Å). The angle of detection ranges from 20° to 120° 2θ for each sample with a total of 7 samples can be loaded into a 7 x multi-changer. A domed and sealable sample holder allows for inert loading.

Room temperature scans were performed with powdered samples of each ribbon following freeze milling in a PMMA dome sample holder.

In situ measurements were made with an Anton Parr high-pressure cell. Powdered samples were loaded inertly in a glove box into the Anton Parr Cell and transferred to the XRD where 3 bar runs under hydrogen and helium were performed up to 500 °C. A number of scans were taken at temperatures corresponding to points of interest according to the DSC results.

The DSC trace for each binary alloy allowed a number of heating points to be chosen for the in situ XRD measurements. They are as follows:

Membrane Heating and Cooling under Hydrogen (°C)

In the attempt to efficiently test and compare samples, specific temperature profiles were chosen to record thermal behaviour, individual to each sample.

Table 1. Key: 'X' Indicates the membrane heating temperature used. Binary 1 is the first ZrCu membrane fabricated, Binary 2 the second ZrCu membrane and Ternary 1 the ZrCuTi membrane composition.

Temperature (°C)	Binary 1	Binary 2	Ternary 1
25			X
30	X	X	
50	X	X	X
100	X	X	X
125	X	X	X
150	X	X	X
175	X		
200	X		X
215	X	X	
225	X		X
250	X	X	X
275	X		X
300	X	X	
350	X		X
400	X	X	X
450	X		X
500	X	X	X
400	X	X	X
300	X	X	X
200	X	X	X
100	X	X	X
30	X	X	X

3.9 Thermal Gravimetric Analysis (TGA)

A Netzsch TG209C Thermo Gravimetric Analyser is situated in an argon glovebox. During heating using a highly sensitive weight balance the TGA detects changes in sample weight. The heat profiles were run from 29 to 400 °C.

4. Results and Discussion – Binary Alloys

4.1 Structure of Melt Spun Ribbons

Two binary (ZrCu) ribbons were successfully fabricated using a single-roller melt spinner. Binary 1 (B1) produced a 5 mm wide continuous ribbon. Binary 2 (B2) produced was an improved 8-10 mm wide and more continuous in structure. B2 was prepared with a slower heating rate and was held for an extended period above the melting point of the alloy ensuring a lower viscosity melt so a better ejection of material onto the copper wheel could be achieved.

Both binary compositions produced similar thickness ribbons where membrane thickness has previously been highlighted as a key factor in performance (Hara et a. 2000, Dolan et al. 2006, Sholl and Hao 2011). Micrometer measurements show B1 and B2 average thickness between 24 and 30 μm. This suggests that, performance-wise, the limiting factor would be bulk diffusivity (Dolan et al. 2006) if a Pd coating were applied to improve hydrogen dissociation/recombination.

Table 2. Ribbon Thickness in μm of B1 and B2

	Point 1 Average (μm)	Point 2 Average (μm)	Point 3 Average (μm)	Overall Average (μm)
B1	25.2 ± 6	24.3 ± 4.5	23.8 ± 3.3	24.4 ± 4.6
B2	27.3 ± 6.1	35.7 ± 7.6	26.1 ± 6.1	29.7 ± 6.6

4.1.1 SEM Analysis

SEM analysis of as-received melt-spun ribbons shows a consistent ribbon structure. Upon increased magnification, amorphous regions were identified using SEI and BEI techniques. B1 shows signs of crystallization after melt spinning, especially evident at high magnification, although this accounted for only a small proportion of the whole ribbon. EDS on each sample identified the ribbon composition.

Binary 1 - ZrCu

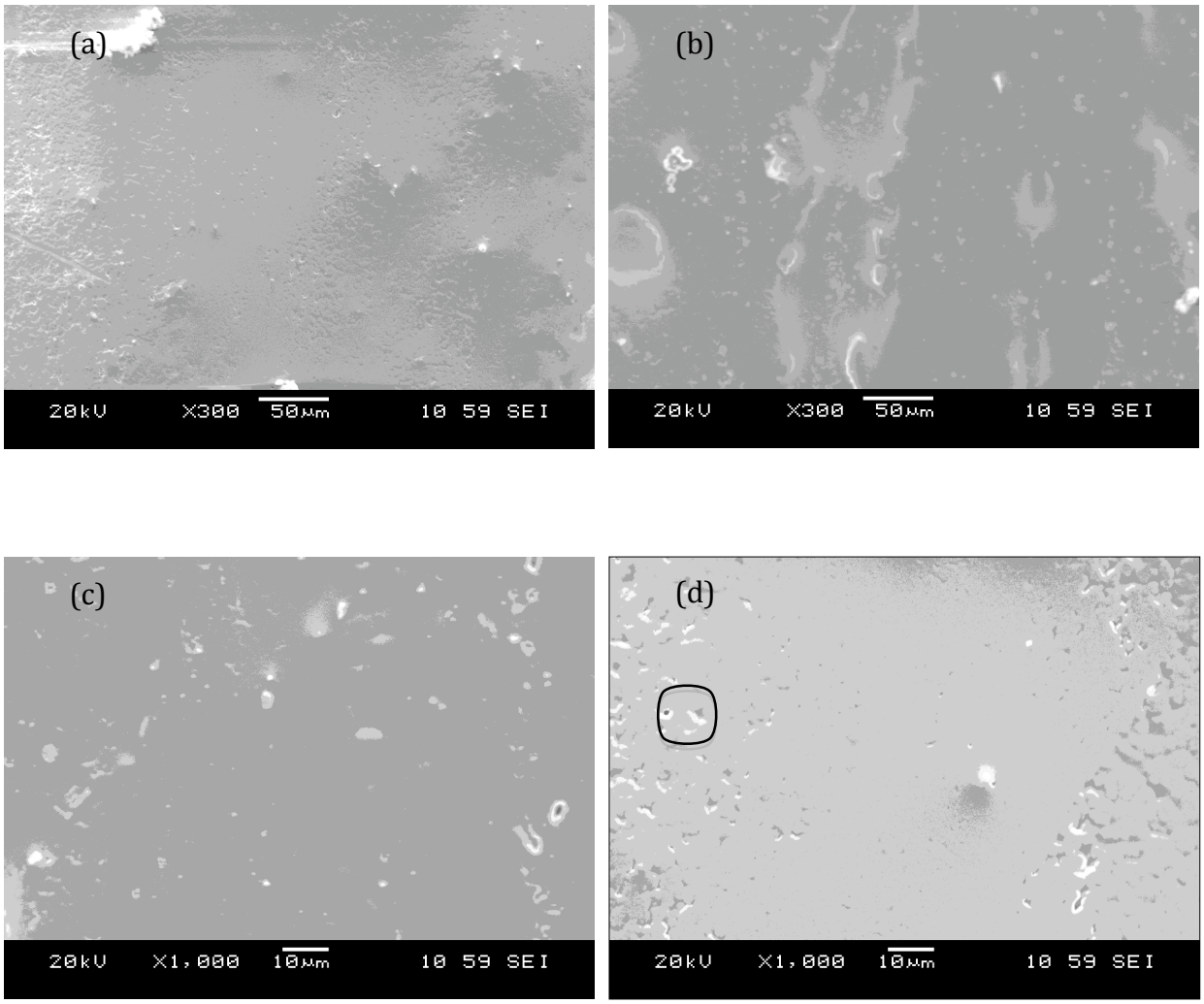

Fig. 5 Room Temperature SEM of B1 (a) at x 300 SIDE A, (b) at x 300 SIDE B, (c) at x 1000 SIDE A and (d) at x 1000 SIDE B

B1 showed a mostly amorphous structure in Figure 5. Upon increased magnification it can be seen in Fig. 5(d) (black square) that grains were formed within the ribbon with an estimated size of 2-5 μm. From further SEM analysis carried out over 12 different point areas, grain formation was apparent along different sections of ribbon but did not dominate the ribbon structure.

Grain formation was nearly exclusively seen on side A, possibly due to being exposed to a slower cooling rate than side B. Side A also shows fewer physical defects than B in both magnifications. This is possibly due to side B hitting the copper wheel surface, which may contain small particles of contamination, and so on a macro-scale altering the physical nature of the ribbon surface as it cools down. This therefore suggests that side A is the free side and that side B is the wheel side of the ribbon when being melt spun.

4.1.2 XRD Analysis

The predominantly amorphous structure was confirmed by XRD measurement (Fig. 6). A large broad peak dominates the pattern. The appearance of zirconium and copper-zirconium peaks within this broader peak, suggest correlation with the areas of grain formation observed using SEM.

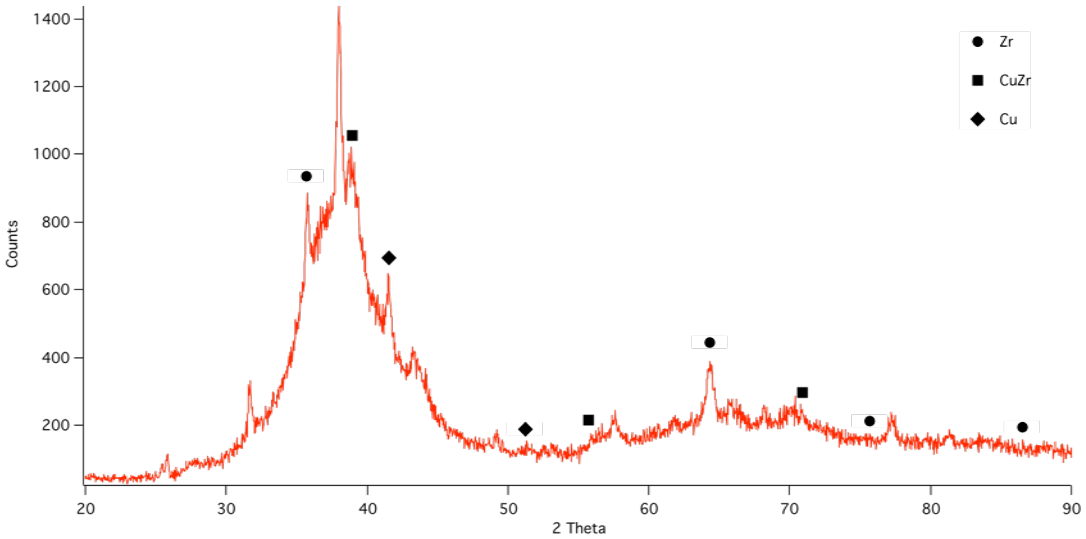

Fig. 6 Room Temperature XRD of B1.

Fig. 6 shows a peak at 37˚ (2-Theta) which has not been labeled. Thorough analysis failed to match any known diffraction data related to this peak and so it is assumed that the peak is due to some impurities that may have contaminated this specific sample during fabrication. The peak disappears on heating to 200 °C.

Binary 2 – ZrCu

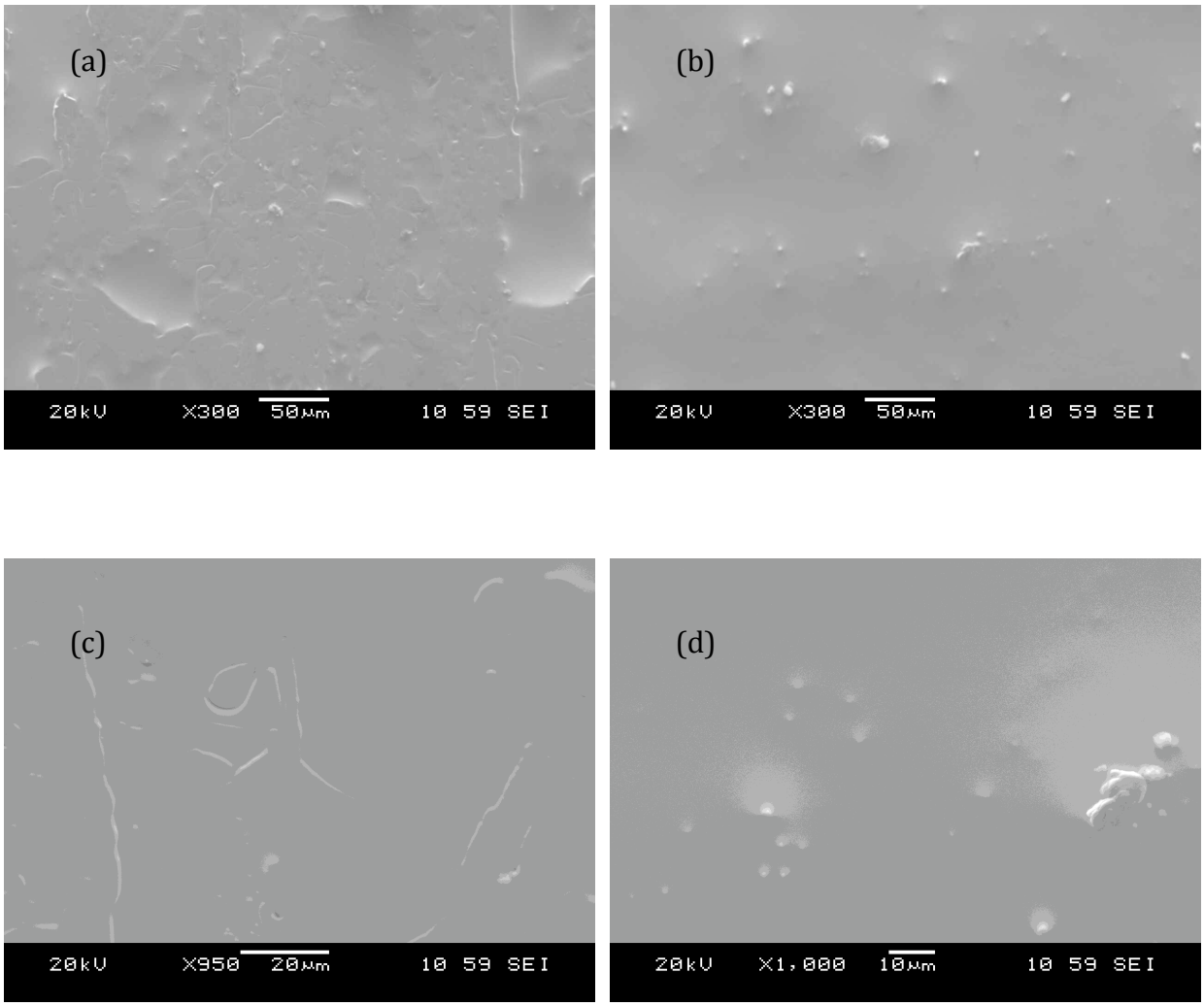

Fig. 7 Room Temperature SEM (a) at x 300 SIDE A, (b) at x 300 SIDE B, (c) at x 1000 SIDE A and (d) at x 1000 SIDE B.

Fig. 7 (a-d) shows that B2 is fully amorphous. Surface topography is of a similar nature to B1, but with no signs of grain formation at either magnification. This indicates that B2 was formed with a sufficient cooling rate for both the free and wheel sides to negate any nucleation and crystallization of grains. This may result from a combination of extended heating time at a slightly higher

temperature above its melting point and an increased thermal heat transfer coefficient due to better thermal contact of the wheel and ribbon. This would allow for an increased cooling rate across the whole sample resulting in less time for crystallization and grain formation (Gillen and Cantor 1985).

Side A of B2 displays the same physical characteristics as side B of B1. The physically rougher surface, with scratch-like indentations, suggests that possible contamination on the wheel surface have affected the topography of the ribbon. Side B also displays more convex surfaces structures, which again would lead to assuming underlying material has affected the surface structure. It is assumed, therefore, that side A of B2 is the wheel side and side B is the free side.

X-ray diffraction data at room temperature shows the existence of the fully amorphous nature of this ribbon (Fig. 8). This correlates with the SEM micrographs showing fully amorphous nature of B2.

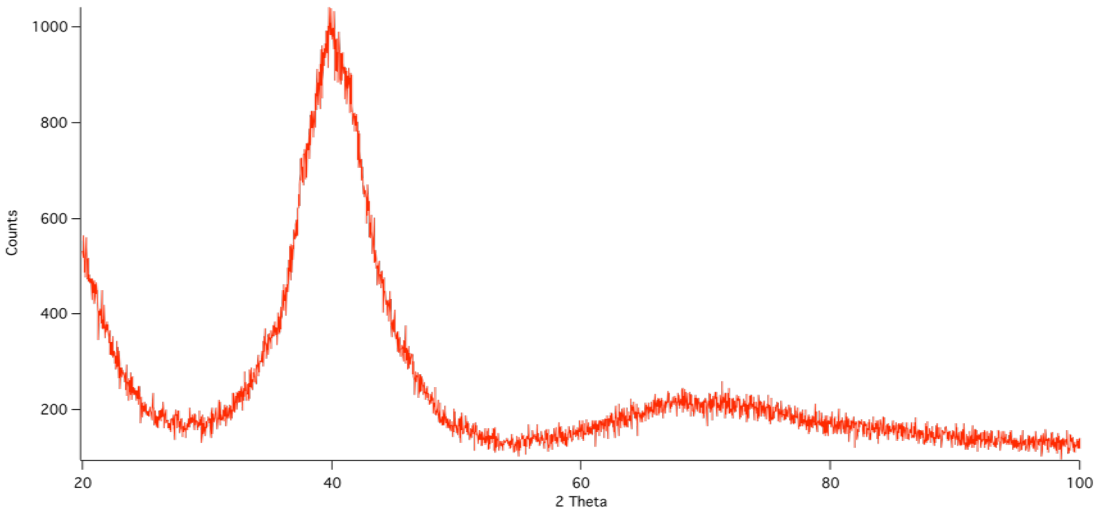

Fig. 8 Room Temperature XRD of B2.

The lack of any significant sharp peaks in Fig. 8 demonstrates a fully amorphous ribbon. The room temperature measurements also provide a reference to compare the variable temperature in-situ measurements that followed and are discussed later.

4.2 Composition of Melt Spun Ribbons

4.2.1 EDS Analysis

EDS analysis data is summarized in Tables 3 - 5 and averaged to identify the overall composition by wt%.

Table 3. EDS weight percent measurements of Zr and Cu on 'free' and 'wheel' ribbon sides (B1) when melt spun and the corresponding positions along the ribbon.

BINARY 1	Zirconium wt%	Copper wt%
Free Side Bottom	56.4	43.6
Free Side Middle	55.57	44.43
Free Side Top	51.09	48.91
Average	**54.35**	**45.65**
Wheel Side Bottom Left	58.65	41.35
Wheel Side Middle	55.03	44.97
Wheel Side Middle Left	54.37	45.63
Average	**56.02**	**43.98**

Table 4. EDS weight percent measurements of Zr and Cu on 'free' and 'wheel' ribbon sides (B2) when melt spun and the corresponding positions on the ribbon.

BINARY 2	Zirconium wt%	Copper wt%
Wheel Side Bottom	56.74	43.26
Wheel Side Middle	55.73	44.27
Wheel Side Top	57.23	42.77
Average	**56.57**	**43.43**
Free Side Top Right	55.65	44.35
Free Side Middle	56.97	43.03
Free Side Bottom	63.05	36.95
Average	**58.56**	**41.44**

Table 5 EDS averaged weight percent measurements of 'free' and 'wheel' ribbon sides. Atomic percent is also calculated.

	Zirconium wt%	Copper wt%	Zirconium at%	Copper at%
Binary 1	55.18	44.82	46.17	53.83
Binary 2	57.57	42.43	48.59	51.41

(a)

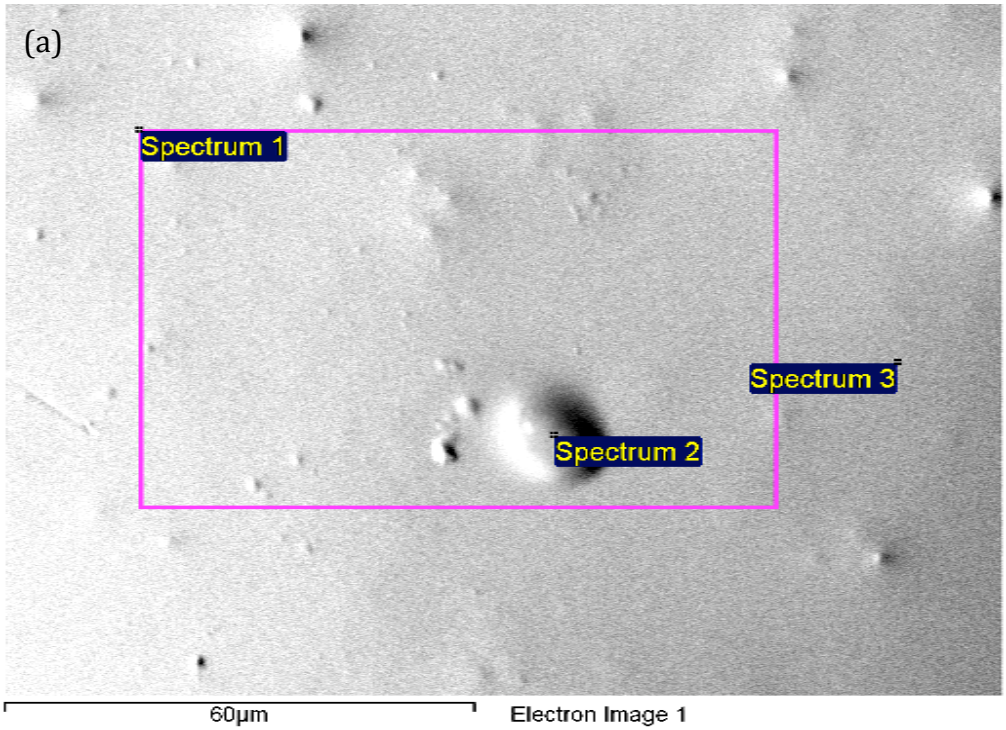

(b)

Processing option : All elements analysed (Normalised)

Spectrum	In stats.	Cu	Zr	Total
Spectrum 1	Yes	42.30	57.70	100.00
Spectrum 2	Yes	26.13	73.87	100.00
Spectrum 3	Yes	42.41	57.59	100.00
Mean		36.95	63.05	100.00
Std. deviation		9.37	9.37	
Max.		42.41	73.87	
Min.		26.13	57.59	

All results in weight%

Fig. 9 EDS analysis of 'free' ribbon side of B2 at the 'bottom' position.

Composition variance across the ribbon is small, ranging only 2-3 wt%. The measurement taken on the free side of B2 at the bottom, however, shows an average weight percent value for the ribbon Zr 63.05% Cu 36.95%. This is over 6 % more Zr than the next closest measurement (56.97%). This value can be explained by the location of this EDS measurement shown in Fig. 9.

Spectrum 2 on Fig. 9 is located on a surface defect caused by the processing method. This type and size of defect, approx. 10 microns, is sparsely distributed along the ribbon. It shows there is a higher concentration of zirconium in the defect (73.87 wt%), possibly caused either by an area with uneven cooling rate where the zirconium solidified before the copper due to its higher melting point, zirconium (1,855 °C) compared to copper (1085 °C). This has subsequently affected the averages of the overall composition. Although not significantly prevalent through out the ribbon structure, these defects are seen across the sample, and are still a part of the composition and so are considered in the compositional measurements.

4.2.2 Crystallisation Temperature

DSC traces shown in Fig. 10 confirm the composition of B1 with a single distinct exothermic peak at 424.9 °C under Ar, with a small broad Tg peak preceding it, correlating to the crystallization temperature in the literature for ZrCu systems (Wang et al, 2002, Ansara et al. 1982, Martinek et al. 2006). B2 has a crystallization temperature (T_x) of 443.6 °C, the slow increase in exothermic behaviour from 150 °C to T_x is due to the structure of the material. B1 shows some degree of crystallization. These microcrystals in fact work as a seed for further crystallization, therefore reducing the crystallisation temperature where solidification starts, and act as centres for further nucleation. Nucleation on these centres is therefore thermodynamically more favourable, (Koster 1988) which is exhibited by the lower crystallization temperature of B1 compared to B2.

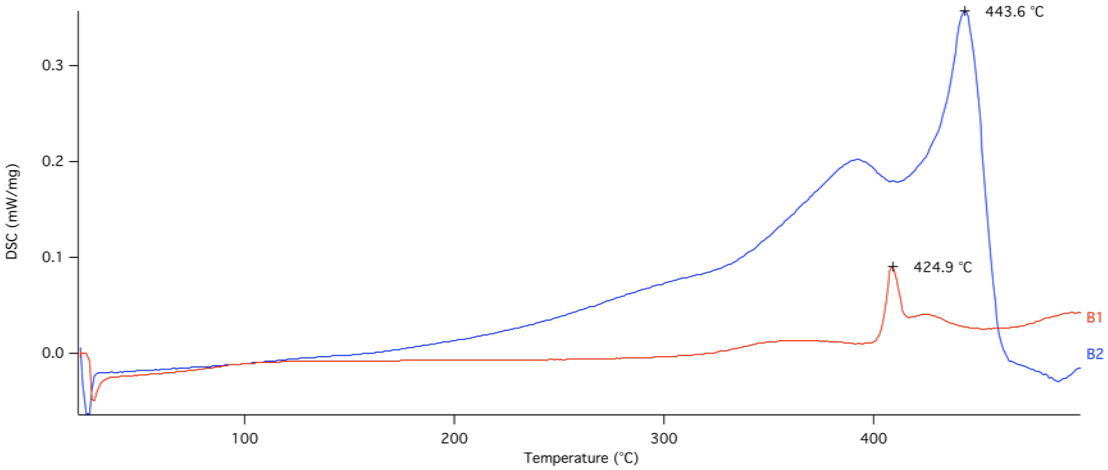

Fig. 10 The 2 DSC traces for B1 and B2 under argon at a heating rate of 2 °C/min.

4.3 Binary Alloy Behaviour under Hydrogen

4.3.1 DSC Analysis

DSC trace shown in Fig. 11 indicates that both binary samples have distinctive thermal profiles specific to each sample composition under argon and hydrogen.

The first hydrogen measurements signify the sample's thermal behaviour when heated under hydrogen up to 500 °C (red trace). The following run on the same sample under argon atmosphere show the corresponding desorption characteristics of each sample (blue).

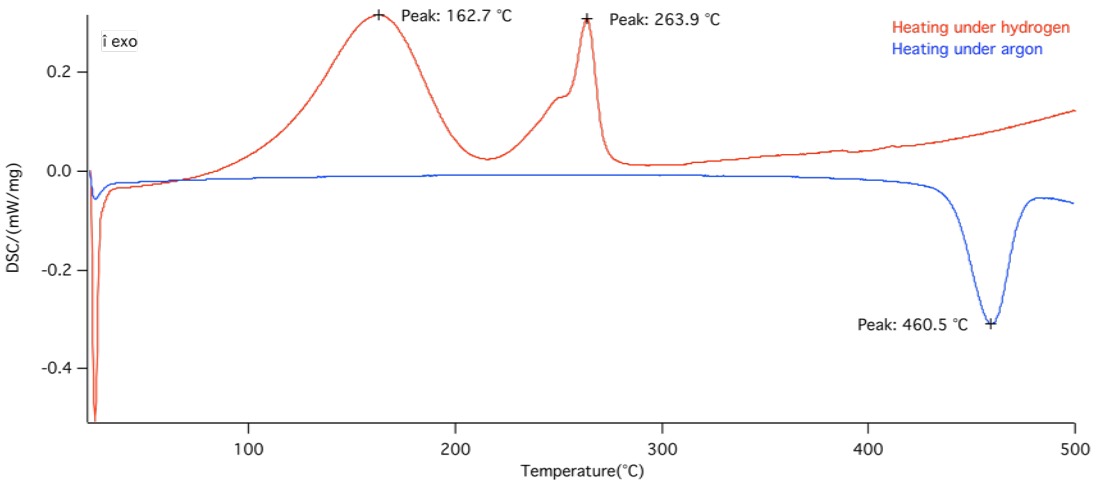

Fig. 11 DSC of B1 under 3 bar hydrogen at 2 °C/min and subsequently under 3 bar argon at 2 °C/min.

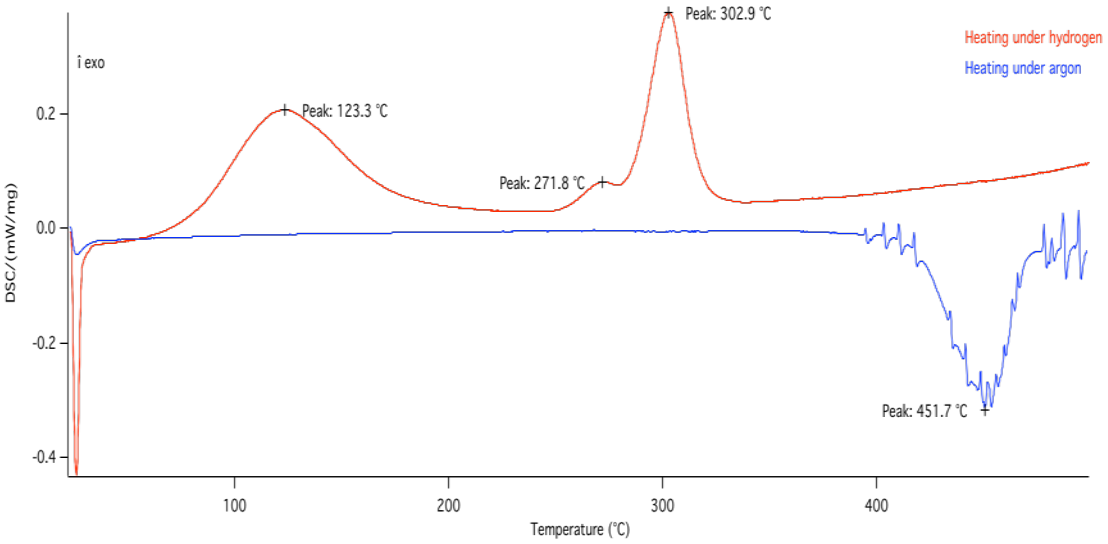

Fig. 12 DSC of B2 under 3 bar hydrogen at 2 °C/min and subsequently under 3 bar argon at 2 °C/min.

Upon heating in hydrogen both samples exhibit two exothermic peaks.

Table 6 DSC profiles for B1 and B2 under 3 bar hydrogen.

	1st exothermic peak (°C)	2nd exothermic peak (°C)
Binary 1	162.7	263.9
Binary 2	123.3	302.9
Difference (°C)	39.4	39

Fig. 12 and Table 6 show that B2 exhibits its first exothermic peak at a lower temperature than B1 and its 2nd peak at a higher temperature. At this point the cause of the 1st peak in both alloys needs further exploration and is investigated later.

It is possible to relate the 2nd exothermic peak under hydrogen conditions to the single endothermic peak under the subsequent argon conditions due to their corresponding peak areas: Under hydrogen B1 exhibits a 2nd exothermic peak at 263.9 °C with a peak area of 171.4 J/g. The endothermic peak under subsequent argon conditions exhibits a peak area of -168.2 J/g. B2 displays a similar relationship. The 2nd exothermic peak at 302.9 °C exhibits a peak area of 230.7 J/g. The endothermic peak, subsequently under argon, exhibits a peak area of -223.7 J/g.

This suggests that the 2nd peak observed during hydrogenation is directly related to the single endothermic peak exhibited with subsequent heating under argon. A hydriding and dehydriding phase or crystallization phase may be assumed to form at the two peaks respectively due to the conditions of the measurements

and the correlation to zirconium hydride formation around 277 °C from the literature (Dini and Dunlap 1985).

The differing energies of the 2nd exothermic peaks of both B1 and B2 compared to their endothermic peaks under argon illustrate that, although small, there is some energy difference due to the hydrogenation process occurring under hydrogen in the 2nd exothermic peak.

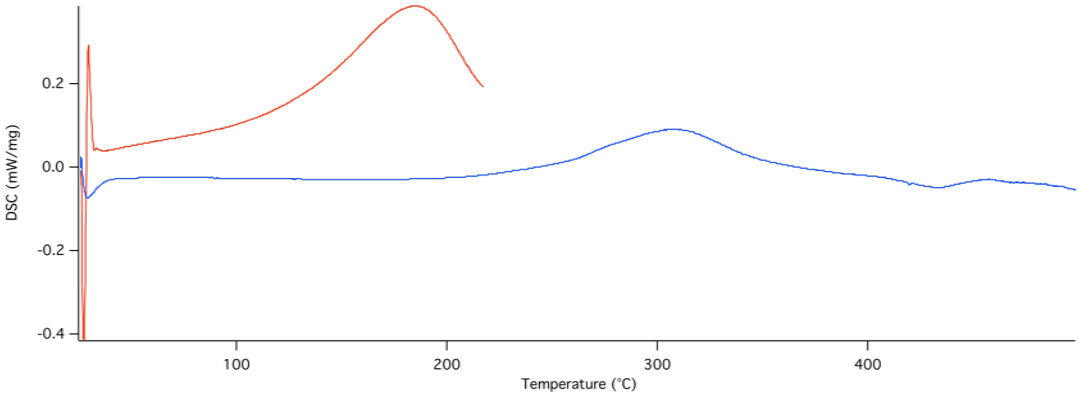

Fig. 13 DSC of B1 under 3 bar hydrogen at 2 °C/min to 217°C (red) and subsequently under 3 bar argon at 2 °C/min to 500°C (blue).

A further DSC measurement was conducted to verify the relationship of the 2nd exothermic peak to the single endothermic peak.

A DSC trace of B1 under hydrogen at 3 bar to 217 °C, cooled and then heated to 500 °C under argon confirms this suggestion. Fig. 13 shows that there is no endothermic peak exhibited during the argon measurement suggesting that the 2nd exothermic peak is related to the endothermic peak and so could represent hydrogenation and dehydrogenation of the sample respectively. The small broad

peak in the blue trace indicates that no definitive crystallization process has occurred and instead a stable hydride has formed. Therefore the first exothermic event observed for B1 under hydrogen may indicate some ordering in the crystal structure (Dini and Dunlap 1985).

To identify the nature of both peaks in both DSC traces, and determine the possible formation of zirconium hydride or other phases, structural analyses were performed under various temperatures by XRD

4.3.2 In-situ XRD Analysis

Binary 1- $Zr_{46}Cu_{54}$

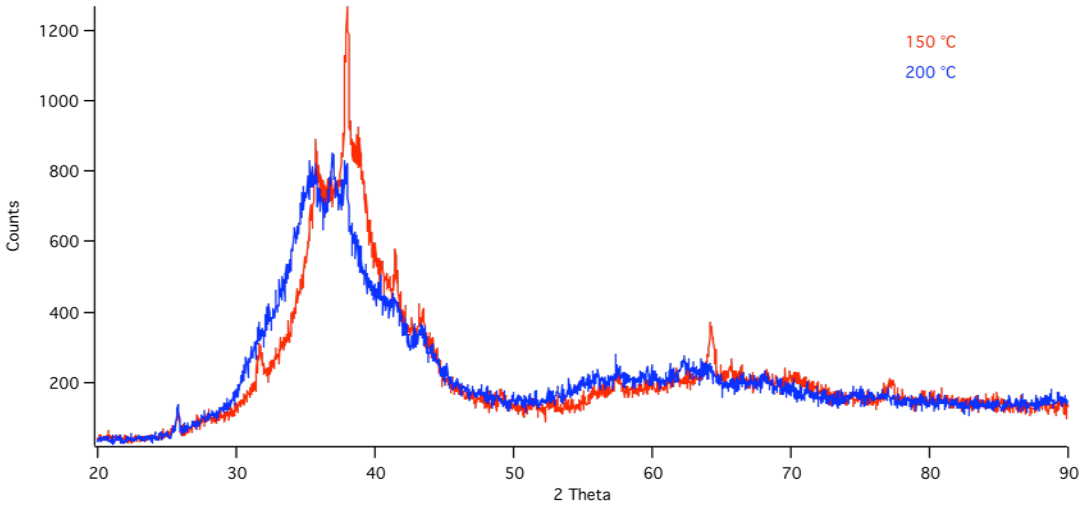

Fig. 14 XRD of B1 under 3 bar hydrogen scans at 150 °C and 200 °C showing a drop and left shift.

The first phase change occurs at 150 °C where the broad peak shifts left on the 2 Theta scale to a lower angle. This shift is associated with the first exothermic peak observed by the DSC trace. As no phase formation is observed it suggests that the 1st exothermic peak is not a hydriding or crystallization phase but a

change in lattice structure due to the influence of hydrogen absorption (Dini and Dunlap 1985).

Although a phase transition looks to have initiated, due to the observation of small peaks, there are only low intensity phases, which suggests there is only a small amount of these phases. High intensity peaks only formed when the temperature reached 200 °C and above. This demonstrates that this temperature is the critical point for a change in thermal stability for B1.

The shift continues until 215 °C where there is a significant exhibition of emerging peaks associated with the formation of $Cu_{1.74}Zr_{2.26}$ (Fig.15).

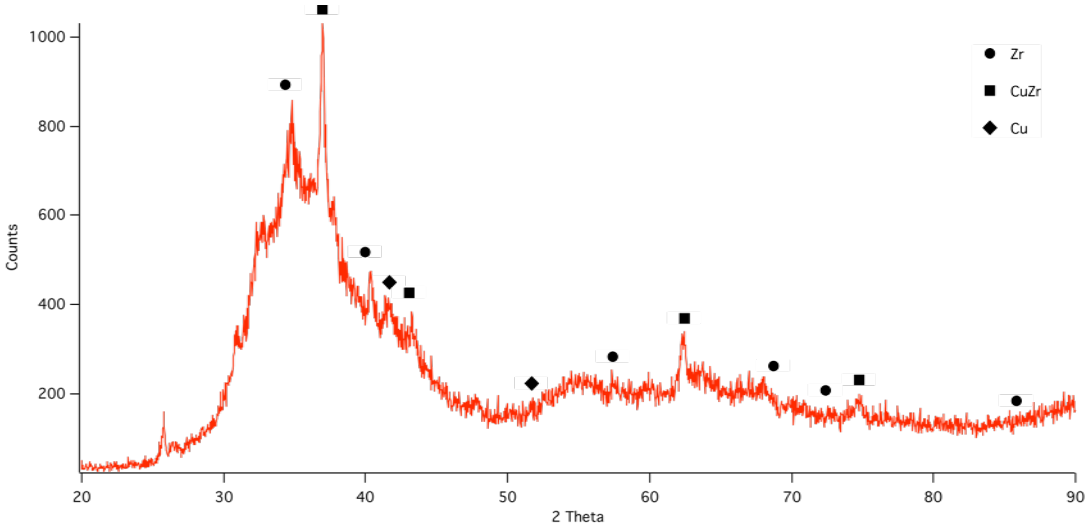

Fig. 15 XRD pattern at 215 °C of B1 under 3 bar hydrogen.

Although there is observation of a CuZr phase initiating there is no correlation of an exothermic crystallization peak with the DSC trace. This suggests that this

may be initiation of crystallization and the start of the phase change from amorphous to crystalline phases.

Typically copper patterns observe a peak at 50° 2 Theta, which is missing from this pattern (Fig. 15). Chung and Liu (2006) have shown that preferential orientation can occur in deposited specimens, heated from low to high temperature. This may explain the absence of a strong peak at 50 ° correlating to a Cu phase observed here. Alternatively it has been considered that the Cu peak may have a low intensity at this temperature.

The XRD pattern collected at 225 °C shows the same 4 phases (Zr, Cu, $Cu_{1.74}Zr_{2.26}$ and amorphous) are observed with the addition of a ZrH_2 phase.

This temperature correlates with the start of the 2nd endothermic peak from the DSC trace (a possible hydriding phase). The XRD pattern supports this suggestion, as a zirconium-hydride phase is present at this temperature Fig. 16.

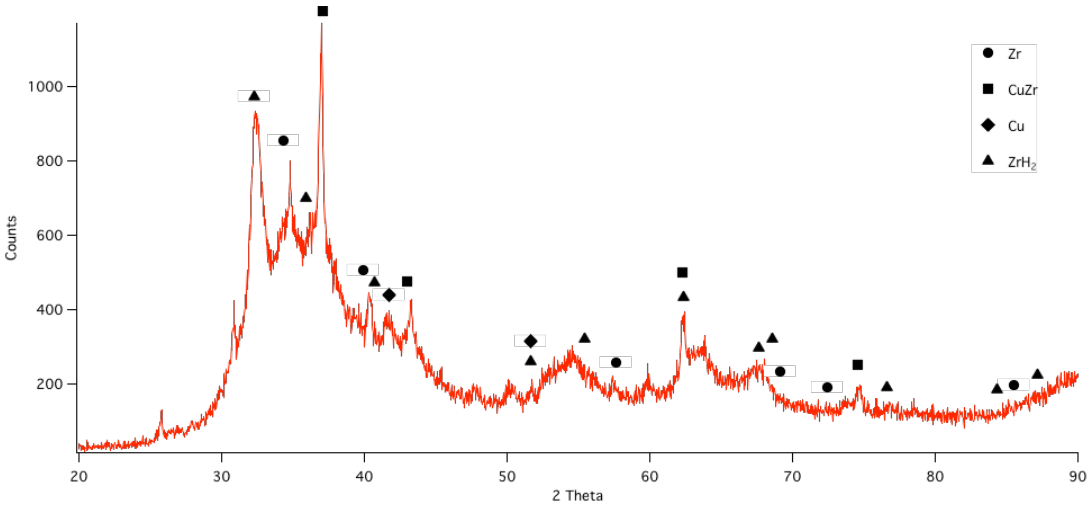

Fig. 16 XRD pattern at 225 °C of B1 under 3 bar hydrogen with new ZrH_2 phase.

Further evidence of continued crystallization of the Zr and CuZr phases is observed with more sharp peaks defined and a shallower amorphous pattern.

The 250 °C pattern (Fig. 17) coincides with the initiation of the 2nd exothermic peak shoulder (Fig. 11). Copper appears to have crystallized further and less of the amorphous phase of the sample is observed.

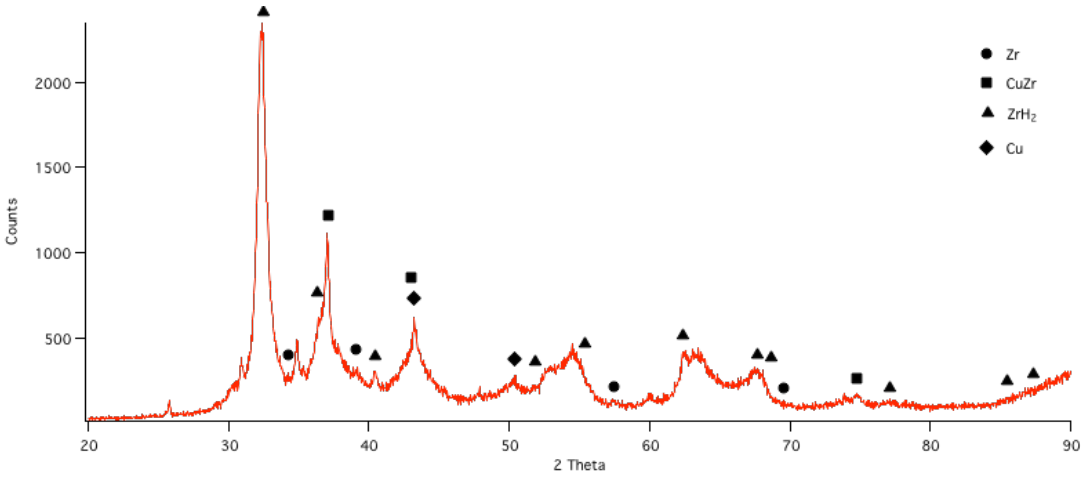

Fig. 17 XRD pattern at 250 °C of B1 under 3 bar hydrogen.

XRD patterns between 250 °C and 275 °C, which correspond to the climax of the 2nd exothermic peak and also its end, show no significant pattern change indicating the bulk of the phase transformation occurs below these temperatures. This identifies the upper limit of any amorphous behaviour before crystallization occurs.

Fig. 18 shows that above 350 °C ZrO has formed, which is a result of either the Anton Parr Cell inadvertently exposing the sample to small volumes of oxygen or gas impurities within the pipeline while at high temperatures and pressure, as hydrides are still observed. This is still under investigation.

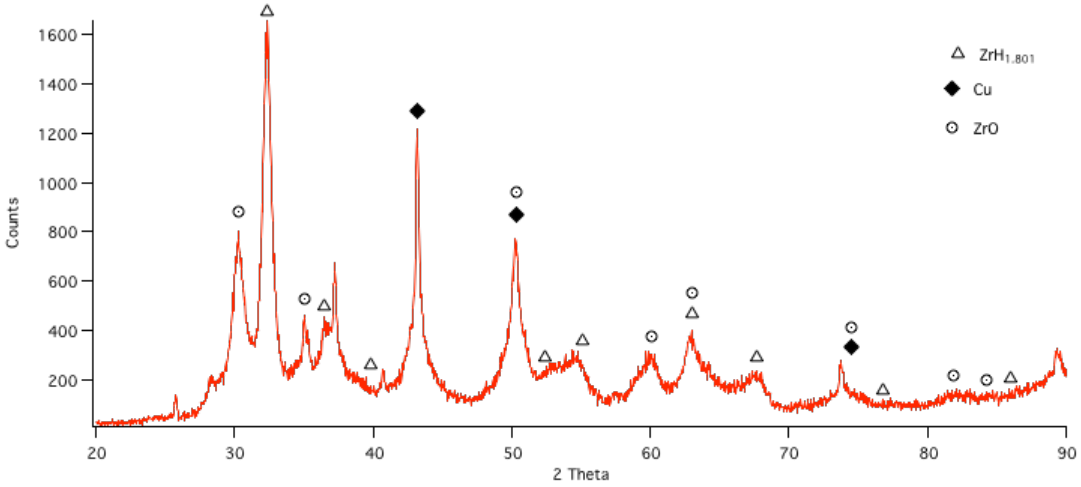

Fig. 18 XRD scan at 350 °C of B1 under 3 bar hydrogen with new ZrO phase.

Binary 2 – Zr58Cu42

Corundum (Al_2O_3) peaks are observed in XRD patterns of B2 sample (Fig. 19). These peaks are continually displayed throughout XRD measurements due to the sample geometry and sample holder.

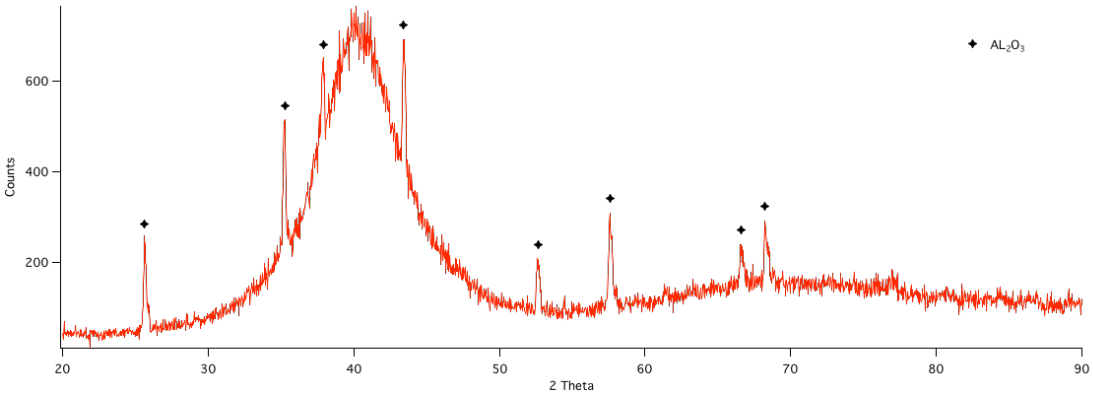

Fig. 19 XRD pattern at room temperature / 30 °C of B2 under 3 bar hydrogen with Al_20_3 phase.

Fig. 19 room temperature XRD pattern of B2 gives reference to the subsequent patterns.

Fig. 20 (XRD Below) shows there is no obvious phase change of the amorphous alloy that corresponds to the 1st endothermic peak (i.e. 123.3 °C), which is consistent with the results from B1.

These patterns, however, indicated a ordering of the crystal lattice as the XRD pattern shifts to the left with a lower angle, similar in trend to B1.

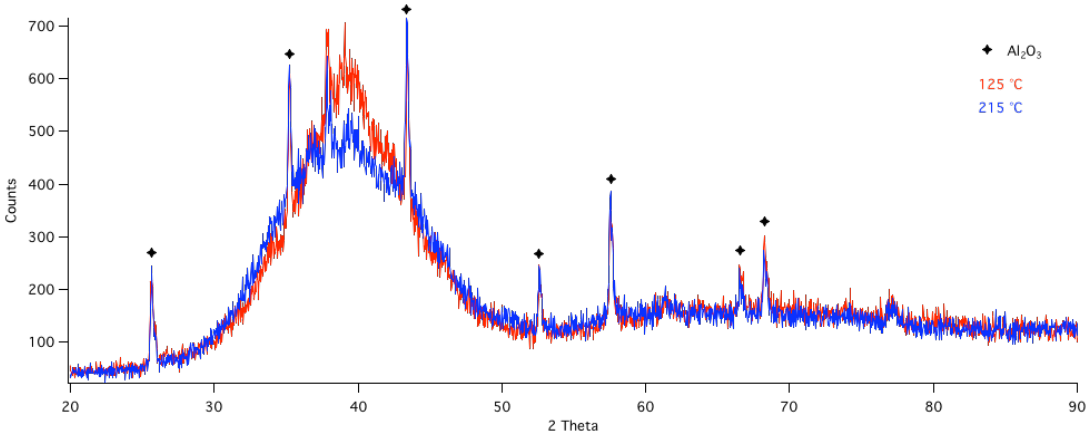

Fig. 20 XRD scans at 125 °C and 215 °C of B2 under 3 bar hydrogen with Al_2O_3 phase showing the downward and slight left shift.

Fig. 21 shows peaks emerging between 200 °C and 250°C indicating the imminent phase forming of copper and low intensity phase indications of zirconium hydride. The new phases relate to the small endothermic peak shouldering the second large exothermic peak on the corresponding DSC trace.

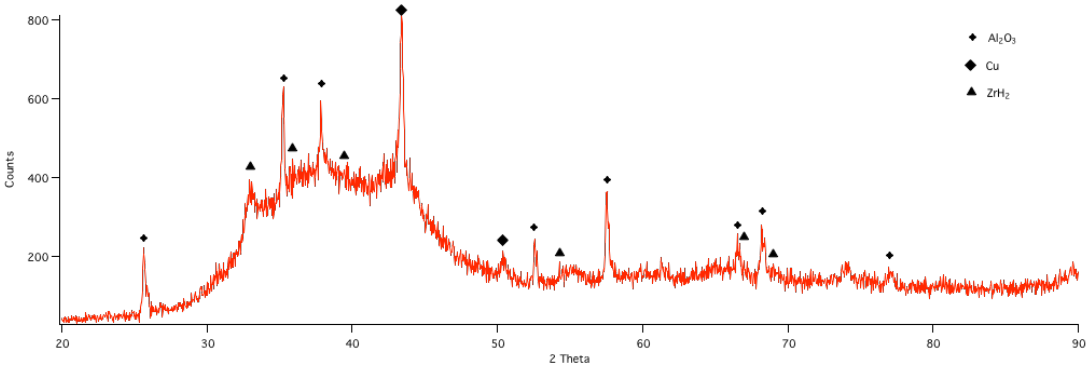

Fig. 21 XRD scan at 250 °C of B2 under 3 bar hydrogen with new ZrH and Cu phases.

ZrH_2 formation at this temperature is comparable to its formation in B1. Both correlate to the initiation of the 2nd exothermic peak from the corresponding DSC trace.

Fig. 22 confirms this relationship of zirconium hydride formation to the 2nd exothermic peak by an increase in temperature to 300 ˚C. This confirms the 2nd endothermic peak relationship to hydrogen uptake with the pattern temperature measured close to the climax of the peak.

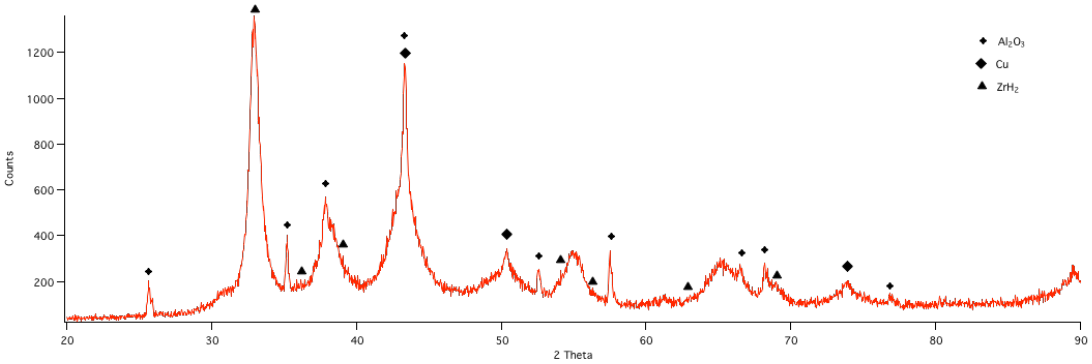

Fig. 22 XRD pattern at 300 °C of B2 under 3 bar hydrogen with ZrH_2, and Cu phases.

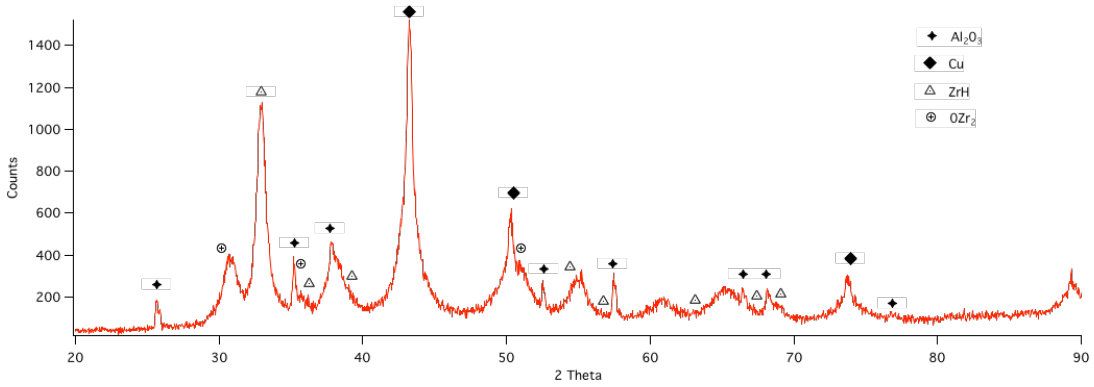

Fig. 23 XRD pattern at 400 °C of B2 under 3 bar hydrogen with zirconium oxide.

Upon increased temperature above 300 °C, as with B1, new peaks indicate the formation of ZrO_2 (Fig. 23 above) which can, again, suggest that there is a possible reaction between residual oxygen within the chamber with Zr. Zirconia is formed at a reaction enthalpy of -1080 kJ/mol (Chase 1988).

$$Zr + O_2 = ZrO_2 \qquad (14)$$

4.3.3 Crystallization Temperature under Hydrogen and Argon

Both binary alloys exhibit exothermic peaks at much lower temperatures under hydrogen (DSC figures) than under argon alone (DSC Ar).

Table 7 shows the crystallization temperatures of B1 and B2 from under argon and hydrogen (also shown in Fig 10).

	Crystallization under Argon (°C)	Crystallization under Hydrogen (°C)
B1	424.9	263.9
B2	443.6	302.9

Table 7 shows the effect of hydrogen on the crystallization temperature. Fig. 11 and 12 display the crystallization temperature under inert conditions and under hydrogen the crystallization temperatures were reduced to 263 °C and 302.9, respectively.

This is a result of the hydrogen absorption into the metal lattice. While hydrogen initially occupies the higher energy binding sites the thermal stability is upheld (the plateau between the peaks) which is important when in operation. However, once filled and lower energy binding sites are used, the hydrogen increases in mobility and the thermal stability decreases (Dolan et al. 2006). This is due to an increase in inter-atomic distance within the alloy (Koster 1996), which destabilizes the membrane structure and can lead to failure. This draws attention to the compromise of increasing thermal stability for operational integrity and the need for high hydrogen mobility and diffusion for permeability.

As increasing zirconium content has been shown to decrease amorphous alloy thermal stability (Inoue et al. 2001, Dolan et al. 2006 and 2009). It would suggest that B2 should have a lower T_x than B1 as it has a higher wt% Zr content. However, B2 exhibited a higher thermal stability under argon with a higher T_x compared to B1, which may improve the ability to resist crystallization and hydriding behaviour. Furthermore B2 was fully amorphous before experimental procedure began compared to small indications of crystallization in B1, which may have facilitated the crystallization phase change for that alloy, lowering the activation temperature needed for crystallization to occur under hydrogen conditions.

4.4 Hydriding Discussion

4.4.1 XRD Shift

A recent study by Endo et al. (2010) observes a single exothermic event under similar conditions to this study. However, the existence of more than one peak in the current study suggests that not only is an alloy-hydrogen phase forming (the second exothermic peak) but also an additional exothermic reaction due to another thermal event (the first exothermic peak) is occurring.

Hydrogenation of B1 and B2 up to 215 °C led to a slight lattice expansion and so a shift in XRD pattern to lower 2-Theta angles (Endo et al. 2010). The change did not coincide with the formation of any new phases (Fig 15 and 20) so at these temperatures it is considered that the alloys are still thermally stable. This suggests that the first exothermic peak is not an additional release of energy for crystallization as suggested by Eliaz and Eliezer (1999) but a lattice structure alteration that keeps the amorphous nature of the alloy intact (Dini and Dunlap 1985).

Originally, phase change was suggested by the exothermic peaks at 162.7 and 123.3 °C for both B1 and B2 respectively by DSC measurements alone (Fig. 11 and 12). However, the corresponding in-situ XRD patterns showed no evidence of any new phase forming for the first exothermic peaks of either binary alloy. The exothermic reaction, therefore, is attributed to a stress relaxation and reordering of the alloy atomic structure (Dini and Dunlap 1985). Natural stresses

in the material exert forces on the atomic structure including defects such as dislocations. When heat was applied, these defects allowed for the movement of metal atoms to reorder the lattice and relax the internal stresses. As the temperature is not at the critical point (T_x) for new crystallization phases to form, the process is undertaken in the amorphous state. Thermal stability of the alloy is therefore maintained at these temperatures and an amorphous state is continued until temperatures reach the crystallization point i.e. temperature for 2nd peak. In addition, amorphous alloys are not thermodynamically favorable to form via melt spinning, therefore stresses, strains and defects are formed which upon heating allow partial ordering of the structure (Dini and Dunlap 1985) but with no definitive phase change as shown in Fig. 14.

The occurrence of the first peak has also been suggested to increase diffusivity due to the structural relaxation of the metallic lattice (Dini and Dunlap 1985), therefore the lower the temperature at which this occurs, the larger the potential operational range is after the peak for applying the membrane to different technologies.

From the in-situ XRD it is apparent that the cause of the 2nd exothermic reaction for both alloys is the absorption of hydrogen into the metal lattice. New phases of ZrH_2 variations are apparent at the corresponding temperatures for each binary alloy. The difference in the phase formation ZrH and $ZrH_{1.8}$ may be due to the compositional variance between the two alloys allowing for differing crystallographic structures to form. However, both show that the 2nd peak is a hydriding phase accompanied by crystallization and is the critical point where

amorphous behaviour is no longer exhibited (Peng et al 2005, Ichitsubo et al. 2005).

4.5 Dehydriding Characteristics

DSC traces of both B1 and B2 display similar endothermic peaks on heating with argon at 3 bar subsequent to hydrogenation. Peak temperatures are similar at 460 °C and 451 °C for B1 and B2, respectively.

4.6 Solubility

In-situ XRD identified that below 220 °C, under 3 bar hydrogen, the sample is mostly amorphous. This is the critical amorphous region for the membrane. IGA measurements below 220 °C, at 1 gauge bar hydrogen (the equipment's capability at the time), were completed to record hydrogen uptake and the membrane's solubility capacity.

Hydrogen solubility was calculated using the following equation:

$$\Delta C = \left\{ \Delta \frac{H}{M} \frac{\rho 22400}{2MA} \right\} \qquad (15)$$

Where ΔC is the hydrogen solubility, H/M is the hydrogen-metal atom ratio, ρ is the membrane density and MA is the molecular weight.

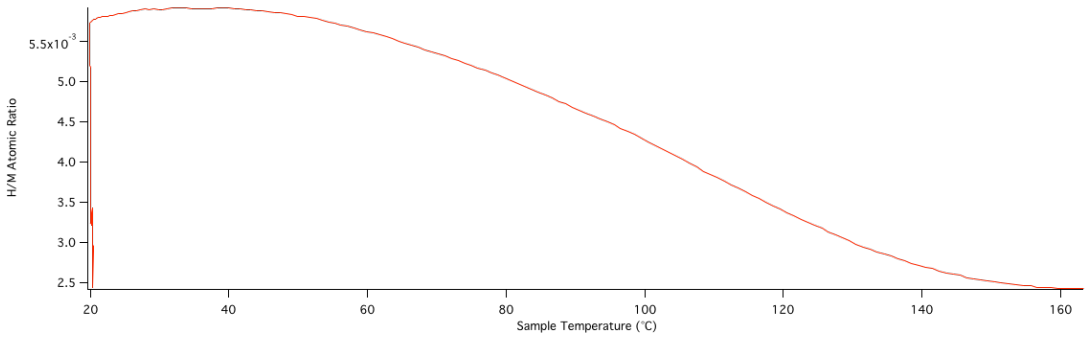

Fig. 24 B1 IGA measurement under 1 bar hydrogen to 217 °C.

The decrease in solubility with increasing temperature (Fig. 24 above) is typical membrane solubility behaviour (Sholl and Hao 2010 and 2011) and is due to the specific amorphous nature where hydrogen occupies spaces in the metal lattice with the highest binding energy first. Once these are occupied, hydrogen binds to sites with a lower binding energy increasing hydrogen mobility, indicating that even with high solubility it is possible to have high diffusivity in amorphous alloys (Dolan et al. 2011).

Table 8 Solubility values at 3 bar between 20 – 215 °C.

Specimen	Solubility (H/M ratio)
B1	0.58
B2	0.72

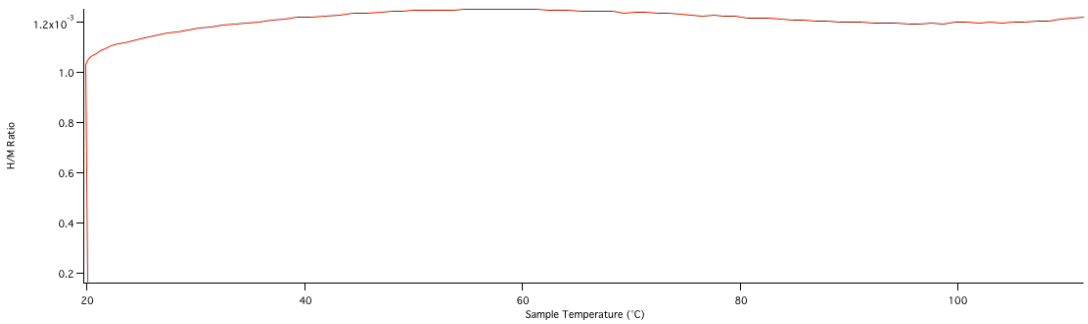

Fig. 25 B2 IGA measurement under 1 bar hydrogen to 217 °C.

The second binary alloy B2 showed a slightly higher solubility of 0.72 (Table 8).

The increase in solubility for B2, $Zr_{49}Cu_{51}$ (Zr58Cu42 wt%), may be a combination of:

1) The decreased content of copper in the alloy (Piper 1966) compared to B1, which has also been shown to decrease hydrogen embrittlement in transition metal alloys, which would be an added benefit for increasing the robustness of the membrane.
2) The degree of crystallinity in B1 compared to B2. The areas of more ordered atoms in B1 will reduce the volume available for the amorphous structure to absorb hydrogen into random binding sites (Yamanaka et al. 2001).

The solubility values are difficult to compare exactly as they are highly dependent on experimental conditions and composition. However, the values for

B1 and B2 compare with Sholl and Hao's calculated predictions for a $Zr_{54}Cu_{46}$ membrane (Sholl and Hao 2011) at 500 K. B2 exhibits a value of 0.58 compared to Sholl's 0.55, which could be due to the slight difference in composition. This suggests that if the ribbons produced were suitable for hydrogen permeability measurements, to test the diffusivity, then this could be a promising membrane alloy.

5. Results and Discussion - Ternary Alloy

A ternary alloy was fabricated to explore the effect of Ti on the ZrCu alloy. This was to investigate hydrogen permeability effects, the possibility of increasing membrane solubility (Shen et al. 2005) and also to have an experimental comparison to a similar theoretical model by Sholl et al. (2011).

A ternary ribbon was successfully produced using a single roller melt spinner. The alloy (ZrCuTi) ribbon was 4-6 mm wide but less continuous than B1 and B2 but of similar thickness.

5.1 Structure of Melt Spun Ribbons

The ternary composition produced a similar membrane thickness to the binary ribbons. Micrometer measurements show T1 average thickness is 16.9 μm. This suggests that, performance-wise, the limiting factor would be bulk diffusivity (Dolan et al. 2006) similar to the binary alloys.

Table 9. Ribbon Thickness in μm of T1.

	Point 1 Average (μm)	Point 2 Average (μm)	Point 3 Average (μm)	Overall Average (μm)
T1	15 ± 3.5	16.4 ± 2.8	19.4 ± 3.6	16.9 ± 3.3

5.1.1 SEM Analysis

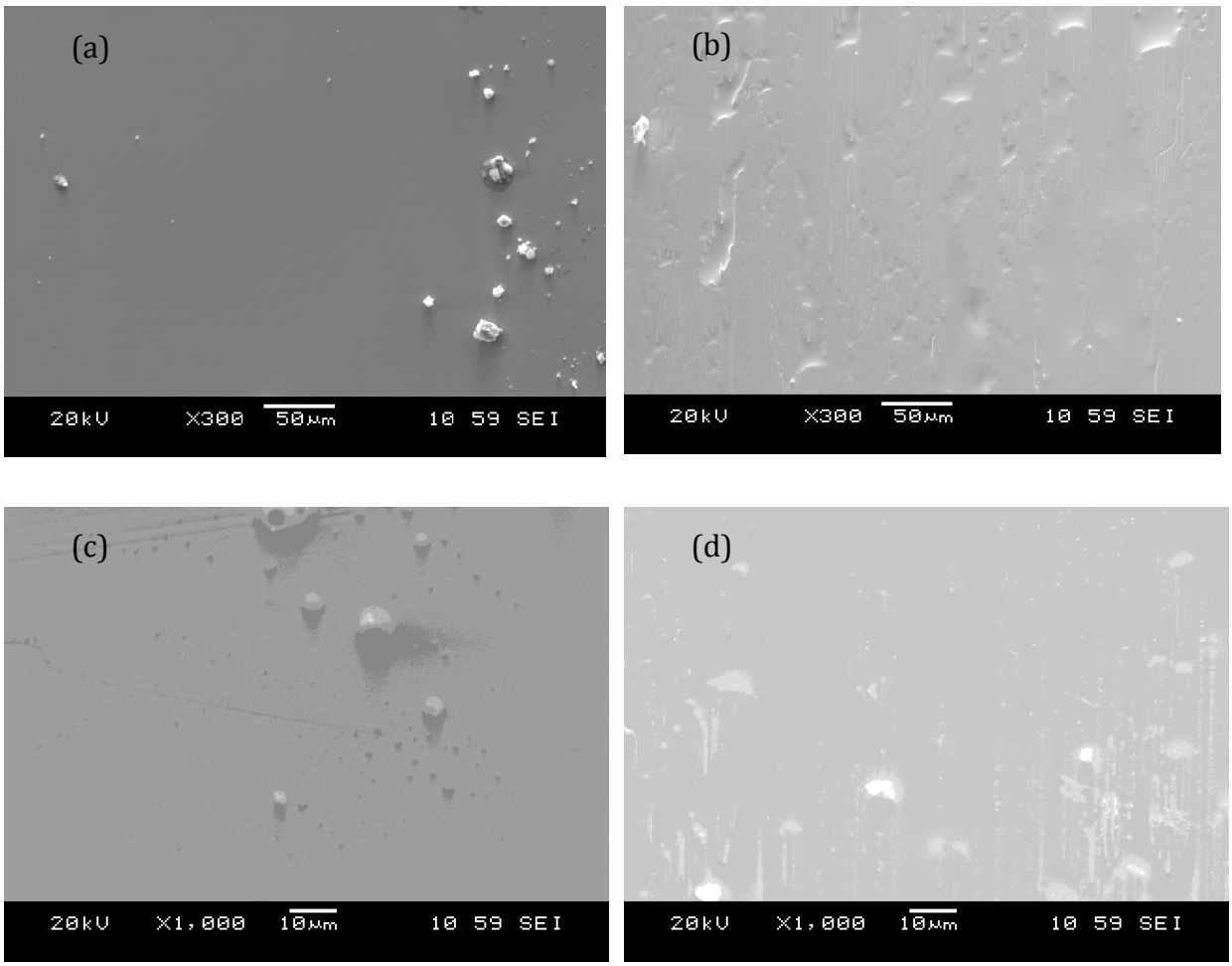

Fig. 26 Room Temperature SEM of T1 at (a) x 300 SIDE A, (b) x 300 SIDE B, (c) x 1000 SIDE A and (d) x 1000 SIDE B.

Figure 26 (a-d) show the ribbon is fully amorphous and exhibits the same surface topography as both binary ribbons. Fig 26 (a), Side A, gives a clear indication that the surface is mostly smooth with convex surface structures distributed randomly. Side B Fig. 26 (b) shows a rougher surface with mostly concave surface structures. The increased magnification images do not appear to show any signs of grain growth, suggesting the ribbon is fully amorphous.

From the similarities of the surface appearance to the binary alloys it is assumed that side A is the free side and side B is the wheel side of the ribbon.

5.1.2 XRD Analysis

Room temperature XRD of T1 exhibits a broad, noisy peak associated with an amorphous material in Fig 27 (below). There are however, distinctive peaks along pattern that may indicate some crystallization has occurred. This is contrary to the 'as fabricated' melt spun ribbon examined by SEM. One possible explanation is that when crushing the ribbon in the freezer-mill to provide powdered materials for XRD, the temperature in one of the milling cycles may have increased due to a lack of liquid nitrogen and so been insufficient to negate the effect of frictional heat in initiating crystallization. Unfortunately there was insufficient sample to repeat the process to avoid this crystallisation.

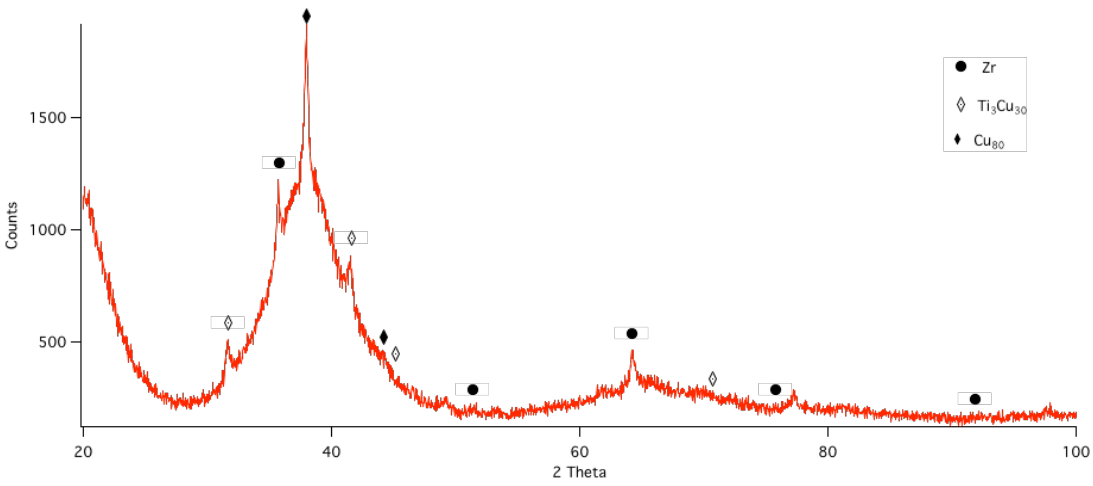

Fig. 27 XRD at room temperature of T1, 70 minute, under helium

5.2 Composition of Melt Spun Ribbons

5.2.1 EDS Analysis

EDS identified the ternary alloy composition. The same method of data collection was used as for B1 and B2.

Table 10 EDS weight percent measurements on the 'free' and 'wheel' ribbon sides (B2) when melt spun and the correlating positions on the ribbon under SEM.

TERNARY 1	Zirconium wt%	Copper wt%	Titanium wt%
Free Side Top	36.74	57.85	7.76
Free Side Middle	37.31	53.51	9.18
Free Side Bottom	25.37	65.45	7.35
Average	**33.14**	**58.94**	**8.01**
Wheel Side Bottom	29.99	60.18	9.79
Wheel Side Middle	34.2	58.5	7.16
Wheel Side Top	34.75	58.16	7.09
Average	**32.98**	**58.94**	**8.01**

Variation in composition for the ternary alloy is increased compared to the binary alloys, due to the increased number of elements. Commonly a variance of 2-5 % is observed.

Measurements again encompassed results from defects as with the binary alloys. One significant change in composition is observed on the ribbon's free side at the

'bottom'. These values again occur from a measurement taken from a similar surface defect to that in B2. Shown in Fig. 30 the defect has a high weight percent of copper, a reduction in the weight percent of zirconium and displayed a similar weight percent of Ti to the other measurements.

(a)

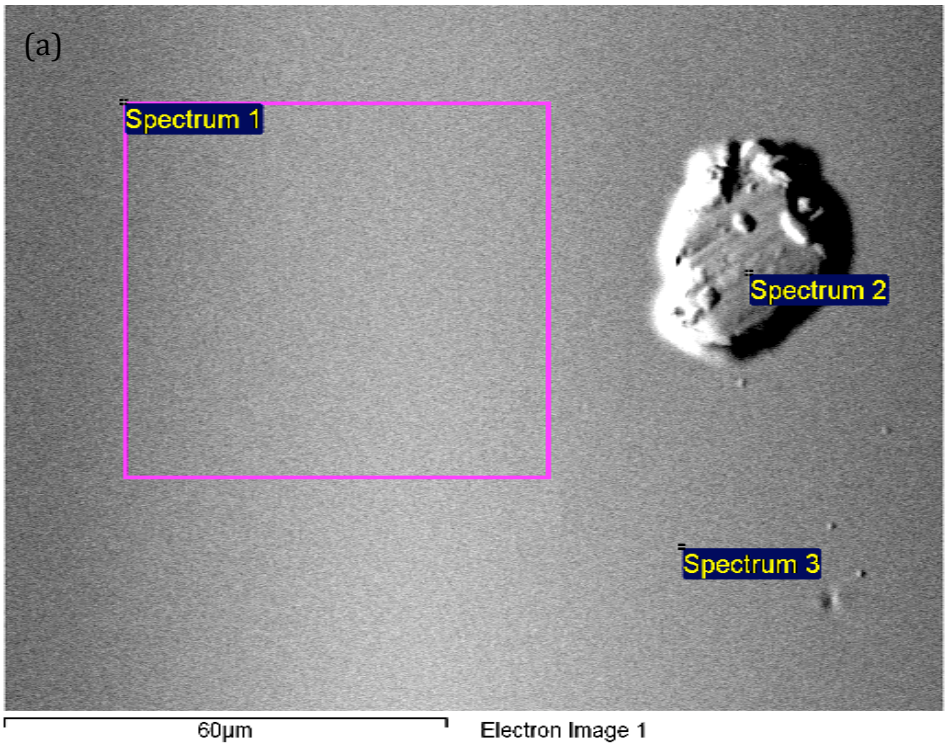

(b)

Processing option : All elements analysed (Normalised)

Spectrum	In stats.	Ti	Cu	Zr	Total
Spectrum 1	Yes	7.23	59.92	32.84	100.00
Spectrum 2	Yes	11.47	77.06	11.48	100.00
Spectrum 3	Yes	7.35	59.37	33.29	100.00
Mean		8.68	65.45	25.87	100.00
Std. deviation		2.41	10.06	12.47	
Max.		11.47	77.06	33.29	
Min.		7.23	59.37	11.48	

All results in weight%

Fig. 28 (a) and (b) EDS of T1 free side 'bottom' of the ribbon, displaying the defect the abnormal value was taken from.

This type of defect is not uncommon but only counts for a small proportion of the complete ribbon structure. The averaging of all the locations and points of measurements within each location produces an accurate measurement of the ribbon composition as a whole.

Table 11 EDS averaged weight percent measurements of 'free' and 'wheel' ribbon sides for T1.

	Zirconium wt%	Copper wt%	Titanium wt%
Ternary 1	33.05	58.94	8.01

The final composition of the ternary alloy is calculated to be Zr33Cu59Ti08 wt% ($Zr_{25}Cu_{64}Ti_{11}$).

5.3 Ternary Alloy Behaviour under Hydrogen

5.3.1 Hydriding and Dehydriding Behaviour

Fig 29 displayed a similar DSC heating profile under hydrogen and argon to the binary alloys.

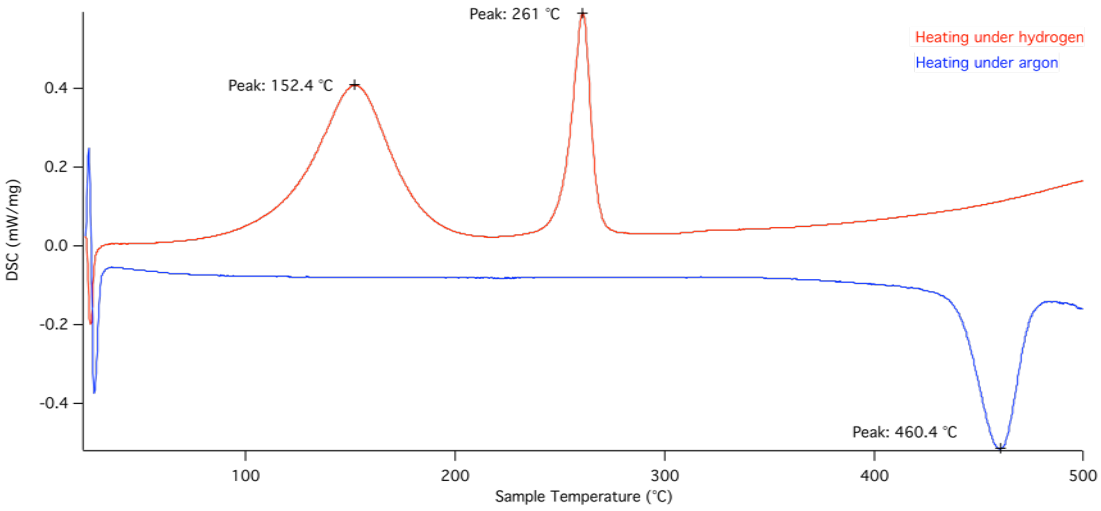

Fig. 29 DSC of T1 under 3 bar hydrogen at 2 K/min and subsequently under 3 bar argon at 2 K/min.

When heating under hydrogen, two exothermic peaks are apparent at 152.4 °C and 261 °C. The first peak occurs at 152.4 °C. This falls between B1 and B2's values for the same exothermic event; 162.7 °C and 123.3 °C. The second peak is almost same for T1 as B1 at 261 °C and 263.1 °C respectively. Both these values are significantly lower than B2's second exothermic peak at 302.9 °C.

T1 also has a smaller plateau between the two peaks, similar to B1 indicating the similar behaviour between lattice ordering to crystallization temperature..

Furthermore, the peak areas of the second exothermic peak under hydrogen and the corresponding single peak exhibited at 460.4 °C under argon do not match as with the binary alloys, 182.8 J/g and -235.8 J/g. This may be due to different hydride formation in T1 compared to B1 and B2 (Fig. 30 below). T1 may have formed an irreversible hydride, which increased the favourability of the alloy to crystallize and so exhibit a lower crystallization temperature under hydrogen than expected (Table 12 below).

Table 12. Crystallisation Temperatures of Binary1 (B1), Binary 2 (B2) and Ternary 1 (T1) membranes.

Sample	B1	B2	T1
Crystallisation Temperature (°C) under Hydrogen	263.9	302.9	261
Crystallisation Temperature (°C) under Argon	424.9	443.6	N/A

5.3.2 In-situ XRD Analysis Under Hydrogen

Fig. 33 shows the first indication of a phase change from the amorphous state occurred at 200 °C.

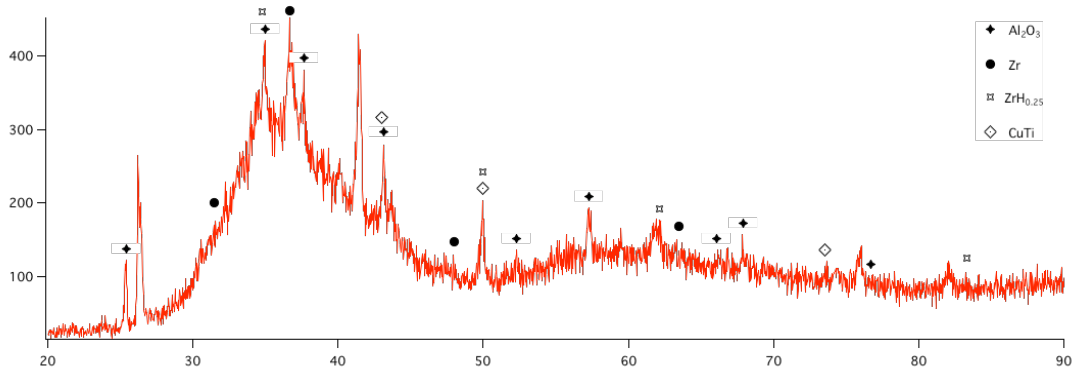

Fig. 30 XRD pattern at 200 °C showing the formation of Zr, $ZrH_{0.25}$ and CuTi phases.

T1 exhibited a left shift in the XRD pattern occurring between 150 and 200 °C, mirroring the lattice ordering behaviour of the binary alloys. This coincides with the later stages of the first exothermic peak shown by the DSC similar to B1 and

B2, which allows the assumption of the same stress relaxation mechanisms occurring.

(As with the previous measurements Al_2O_3 is identified as the sample holder).

The initiation of phase evolution is apparent at 200 °C Fig. 30.

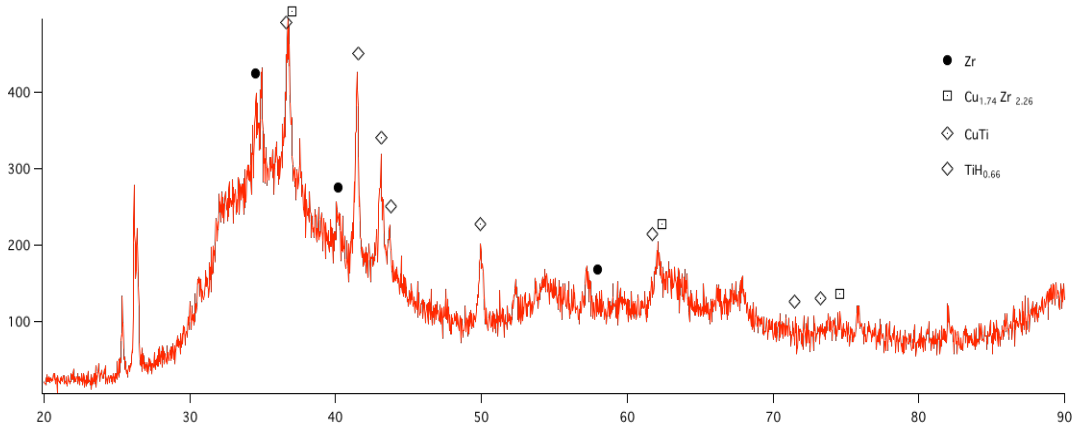

Fig. 31 XRD pattern at 225 °C showing the formation of copper –zirconium.

At 225 °C (Fig. 31 above) B1 showed copper-zirconium had crystallized, this is not apparent for T1 definitively until 250 °C. The introduction of Ti, therefore seems to have stabilized copper and resisted its crystallization and increased its interaction with both Zr and hydrogen. Shen et al (2005) have found that Ti addition can lead to a decrease in onset crystallization temperature in Zr-Cu-Ti systems but an increase in membrane solubility, this could be beneficial in optimising the membrane performance at lower temperatures. Ti addition for Cu was also said to improve amorphous phase formation and promote icosahedral phases during devitrification. This phase formation in the undercooled liquid was then believed to create a barrier against the nucleation

of the Zr_2Cu phase upon heating (Shen et al. 2005). This could explain the difference in phase formation of T1 to B1.

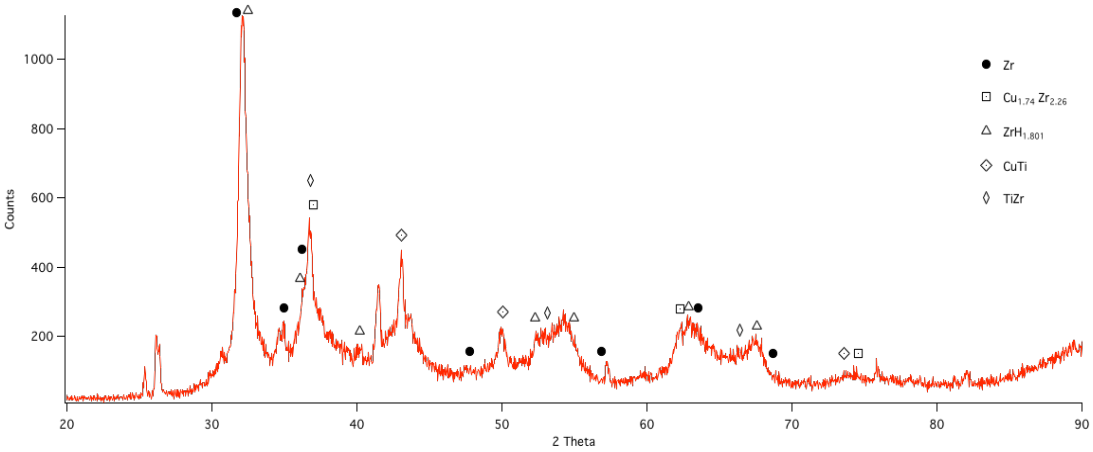

Fig. 32 XRD pattern at 250 °C showing the formation of $Cu_{1.74}Zr_{2.26}$, $ZrH_{1.80}$ and TiZr phases.

At 250 °C (Fig. 32) the phase change is more definitive and clear, with more concise peaks indicating a significant reduction in the amorphous phase. This coincides with the beginning of the second exothermic peak and, considering the new phases that are forming, suggests that this may be a zirconium based phase change.

Fig. 32 shows an increase in crystalline phases within the material. New phases formed by 250 °C include $Cu_{1.74}Zr_{2.26}$, TiZr and an alternate zirconium hydride

Fig. 33 shows a new phase was also seen at 350 °C. Titanium hydride was formed.

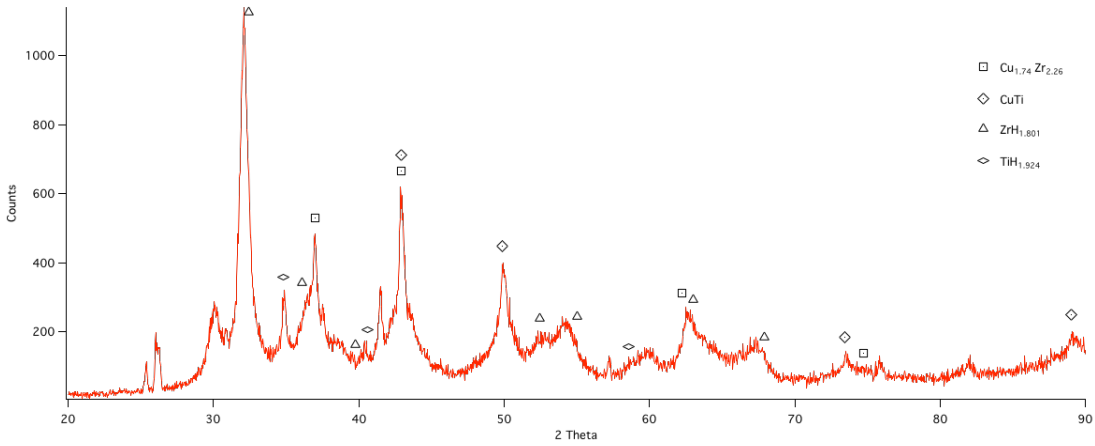

Fig. 33 XRD pattern at 350 °C showing the formation of Zr, $ZrH_{0.25}$ and CuTi phases.

The last significant shift in crystallography is seen at 500 °C Fig. 33. This a large change in the intensity of the peaks as crystallization continues.

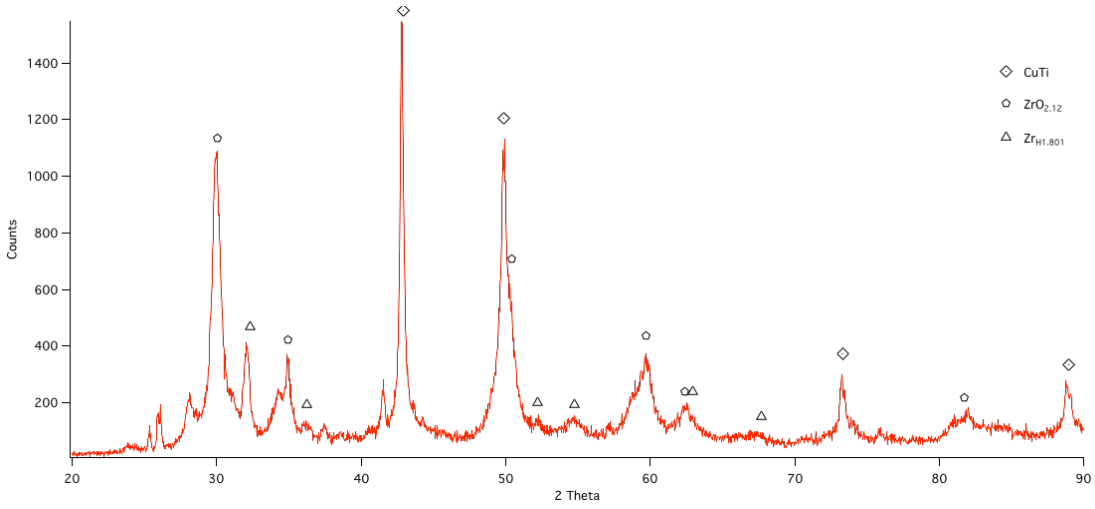

Fig. 34 XRD pattern at 500 °C showing the formation of Zr, $ZrH_{0.25}$ and CuTi phases.

Upon cooling under hydrogen there were no significant changes in the XRD measurements.

5.4 Ternary Discussion and link to Binary Alloys

The DSC trace shows a heating profile similar to both B1 and B2 within a similar temperature range. Through analyzing the data the same mechanisms for stress relaxation for the 1st peak and crystallization and hydride formation for the 2nd peak can be assumed.

It has previously been shown that the addition of Ti to ZrCu amorphous systems decreased the T_x, T_g, and ΔT_x (Shen et al. 2005, Inoue et al. 2001), which is comparable of T1 to B2 in this study. B1 and T1 may have been more comparable if both samples were fully amorphous before experimentation as it is unknown how much the degree of the small crystallization formed prior to testing contributed to the two exothermic peak temperatures.

The two peak positions of T1 are the closest of any of the alloys in this study and correspond with the lowest crystallization temperature. This suggests that not only has the addition of titanium affected the absolute thermal behaviour of the alloy but also has reduced the plateau between the peaks and reduced the operational range under an amorphous structure. This concurs with previous investigations in Ti addition where its addition decreased the resistance to crystallization (Shen et al 2005, Inoue et al. 2001). The presence of crystallization in the starting material before DSC analysis began means that the subsequent thermal analysis may not be a true indicator of a fully amorphous ZrCuTi alloy, facilitating the reduction of the specimen's crystallization temperature. However, even with this effect of the alloying element it has been shown (Inoue et al. 2001) that the addition of Ti to ZrCu based amorphous alloys

improves tensile stress and stress elongation. This could be a vital criterion in advancing transition metal membranes to long life components and highlights the need for careful and considered compromise of alloying elements.

6. Conclusions

Two binary amorphous alloys of Zr55Cu45 wt% / $Zr_{46}Cu_{54}$ (B1) and Zr58Cu42 wt% / $Zr_{49}Cu_{51}$ (B2) were fabricated to determine their thermal behaviour and potential as a hydrogen separation membrane. The first binary (B1) exhibited conventional thermal characteristics with a crystallization temperature close to 300 °C under hydrogen and B2 just over 300 °C. This was confirmed with XRD measurement.

Both also exhibited an additional stress relaxation exothermic event at 162.7 °C and 123.3 °C respectively, which was linked to a structural lattice change, believed to aid in hydrogen diffusion (Dini and Dunlap 1985).

Hydrogen uptake in both B1 and B2 was seen below 220 °C with an increase in H/M ratio which could be increased with increasing gaseous pressure to 0.58 and 0.72 H/M for B1 and B2 respectively. The increase in solubility of B2 was put down to either the increased copper content (Piper 1986) or the degree of crystallinity in the original sample, or both.

The ternary alloy (Zr33Cu59Ti8 wt% / $Zr_{25}Cu_{64}Ti_{11}$) formed a more amorphous alloy than B1 as predicted by (Shen at al. 2005). T1 also exhibited similar thermal behaviour to the binary alloys under 3 bar hydrogen including the additional thermal stress relaxation event. XRD analysis showed later formation of Zr-Cu phases compared to B1, suggesting a stabilisation of the zirconium phase by Ti.

7. Future Work

- Fabricate wide ribbons suitable for hydrogen permeability measurement.
- Identify the robustness of the membranes with physical bending tests and tests using feed streams containing impurities as completed by Inoue (2001) on rods investigating tensile strength and strain elongation.
- Measure hydrogen permeability and compare each alloy.
- Investigate the influence on increased Ti concentration on thermal stability and hydrogen permeability.

8. References

Adhikari, S., & Fernando, S. (2006). Hydrogen Membrane Separation Techniques. *Industrial & Engineering Chemistry Research*, *45*(3), 875-881. doi:10.1021/ie050644l.

Andzelm, J., & Salahub D., (1987), Cluster calculations for diffusion on and in transition metals. *Physics and Chemistry of small clusters*, p 867 – 879.

Ansara, I., Pasturel, A., & Buschow, K. H. J. (1982). Enthalpy Effects in Amorphous Alloys and Intermetallic Compounds in the System Zr-Cu. *physica status solidi (a)*, *69*(2), 447-453.

Antoniazzi, A. B., Haasz, A. A., & Stangeby, P, C., (1989), The effect of adsorbed carbon and sulphur on hydrogen permeation through palladium. *Journal of Nuclear Materials*, 162: 1065 – 1070.

Armor, J. N., (2013), Emerging importance of shale gas to both the energy and chemicals landscape. *Journal of Energy Chemistry*, 22.1: 21-26.

BP Sustainability Report 2012 (2012), Sustainability Review, [online], Available from:http://www.bp.com/content/dam/bp/pdf/sustainability/group-reports/BP_Sustainability_Review_2012.pdf, [Accessed on 12th April 2013].

Cahn, R. W., (1983) *Physical Metallurgy,* Third edition, Elsevier Science Publishers B.V.

Chase, M. W., Jr (1988), NIST-JANAF Thermochemical tables, fourth edition, Journal of Physics and Chemistry, Monography 9, 1-1951.

Chin, H.-S., Suh, J.-Y., Park, K.-W., Lee, W., & Fleury, E. (2011). Hydrogen permeability of glass-forming Ni-Nb-Zr-Ta crystalline membranes. *Metals and Materials International*, *17*(4), 541-545. doi:10.1007/s12540-011-0802-z.

Chung, H. C., & Liu, C. P. (2006). Effect of crystallinity and preferred orientation of Ta< sub> 2</sub> N films on diffusion barrier properties for copper metallization. *Surface and Coatings Technology*, *200*(10), 3122-3126.

Dini, K., & Dunlap, R. A. (1985). Crystallisation and hydrogen absorption in amorphous Cu60Zr40 and Cu50Zr50. *Journal of Physics F: Metal Physics*, *15*(2), 273.

Dolan, M. D. (2010). Non-Pd BCC alloy membranes for industrial hydrogen separation. *Journal of Membrane Science*, *362*(1-2), 12-28. Elsevier B.V. doi:10.1016/j.memsci.2010.06.068.

Dolan, M. D., Dave, N. C., Ilyushechkin, A. Y., Morpeth, L. D., & Mclennan, K. G. (2006). Composition and operation of hydrogen-selective amorphous alloy

membranes. *Journal of Membrane Science*, *285*, 30-55. doi:10.1016/j.memsci.2006.09.014.

Dolan, M., Dave, N., Morpeth, L., Donelson, R., Liang, D., Kellam, M., & Song, S. (2009). Ni-based amorphous alloy membranes for hydrogen separation at 400°C. *Journal of Membrane Science*, *326*(2), 549-555. doi:10.1016/j.memsci.2008.10.030.

Dolan, M. D., Song, G., Liang, D., Kellam, M. E., Chandra, D., & Lamb, J. H. (2011). Hydrogen transport through V85Ni10M5 alloy membranes. *Journal of Membrane Science*, *373*(1-2), 14-19. Elsevier B.V. doi:10.1016/j.memsci.2011.02.028.

Dos Santos, D. S., & Miranda. D. P. E. V., (1997). Hydrogen diffusivity and solubility in crystalline and amorphous alloys. *Journal of Materials Science 32,* 6311-6315.

Eberhard, M., & Tarpenning, M., (2007), The 21st century electric car. *Retrieved July 2* (2006): 2012.

Eliaz, N., & Eliezer, D. (1999). An overview of hydrogen interaction with amorphous alloys. *Advanced Performance Materials*, *6*(1), 5-31.

Endo, N., Kameoka, S., Tsai, P. A., Lingling, Z., Hirata, T., & Nishimura, C., (2010) Hydrogen absorption in the intermetallic compounds Zr_2TM (TM = Cu, Ag and Au) with $MoSi_2$-type structure ($C11_b$), *Journal of Alloys and Compounds*, 490: 124 – 127.

European Commission MEMO, (2003), Kyoto protocol, [online], Brussels, Available from: http://europa.eu/rapid/press-release_MEMO-03-154_en.htm, [Accessed on 22nd January 2013].

Frost, C. B., & Robinson, M. (2007). The Application of Ultra-Thin Palladium Alloy Metal Foils in Gas-Phase Hydrogen Separation or Purification. *Journal of Materials*, (December), 63-64.

Gillen, A. G., & Cantor, B. (1985). Photocalorimetric cooling rate measurements on a Ni-5 wt% A1 alloy rapidly solidified by melt spinning. *Acta Metallurgica*, *33*(10), 1813-1825.

Hara, S., Hatakeyama, N., Itoh, N., Kimurab, H., & Inoueb, A. (2002). Hydrogen permeation through palladium-coated amorphous Zr-M-Ni (M = Ti , Hf) alloy membranes. *Journal of Desalination*, *144*, 115-120.

Hara, S., Sakaki, K., Itoh, N., Kimura, H.-M., Asami, K., & Inoue, a. (2000). An amorphous alloy membrane without noble metals for gaseous hydrogen separation. *Journal of Membrane Science*, *164*(1-2), 289-294. doi:10.1016/S0376-7388(99)00192-1.

Hao, S., & Sholl, D. S. (2008). Using first-principles calculations to accelerate materials discovery for hydrogen purification membranes by modeling amorphous metals. *Energy Environmental Science*, *1*(1), 175-183. doi:10.1039/b806909n.

Hao, S., & Sholl, D. S. (2010). Comparison of first principles calculations and experiments for hydrogen permeation through amorphous ZrNi and ZrNiNb films. *Journal of Membrane Science*, *350*(1-2), 402-409. doi:10.1016/j.memsci.2010.01.017.

Hao, S., Widom, M., & Sholl, D. S. (2009). Probing hydrogen interactions with amorphous metals using first-principles calculations. *Journal of physics. Condensed matter : an Institute of Physics journal*, *21*(11), 115402. doi:10.1088/0953-8984/21/11/115402.

Hinchecliffe, A. B., & Porter, K. E., (2000), A comparison of membrane separation and distillation. *Chemical Engineering Research and Design*. 78.2: 255 – 268.

Holleck, G. L., (1969), Diffusion and solubility of hydrogen in palladium and palladium-silver alloys. *The Journal of Physical Chemistry*, 74.3: 503 – 511.

Horikawa, K., Yamaue, K., & Kobayashi, H. (2010). Response of Hydrogen-Induced Bending Deformation in ZrNi Amorphous Membranes. *Materials Transactions*, *51*(12), 2181-2187. doi:10.2320/matertrans.M2010237.

Inoue, A., Zhang, W., Zhang, T., & Kurosaka, K. (2001). High-strength Cu-based bulk glassy alloys in Cu–Zr–Ti and Cu–Hf–Ti ternary systems. *Acta Materialia*, *49*(14), 2645-2652.

Ichitsubo, T., Matsubara, E., Saida, J., & Chen, H. S. (2005). Local structure and glass transition in Zr-based binary amorphous alloys. *Materials transactions*, *46*(10), 2282-2286.

Jayalakshmi, S., Choi, Y. G., Kim, Y. C., Kim, Y. B., & Fleury, E. (2010). Hydrogenation properties of Ni-Nb-Zr–Ta amorphous ribbons. *Intermetallics*, *18*(10), 1988-1993. Elsevier Ltd. doi:10.1016/j.intermet.2010.03.001.

Kikuchi, E., (1995), Palladium/ceramic membranes for selective hydrogen permeation and their application to membrane reactor. *Catalysis Today 25*, 333-337.

Knapton, A. G., (1977), Palladium alloys for hydrogen diffusion membranes – a review of high permeability materials. *Platinum Met. Rev, 21(2), 44*.

Köster, U. (1988). Surface crystallization of metallic glasses. *Materials Science and Engineering*, *97*, 233-239.

Köster, U., Meinhardt, J., Roos, S., & Liebertz, H. (1996). Formation of quasicrystals in bulk glass forming Zr–Cu–Ni–Al alloys. *Applied physics letters*, *69*, 179.

Marbán, G., & Valdés-Solís, T. (2007). Towards the hydrogen economy?. *International Journal of Hydrogen Energy*, *32*(12), 1625-1637.

Martinek, T., Molnar, A., Katona, T., Bartok, M., & Lovas, A., (1996), Amorphous alloy catalysis IX. Isomerization and hydrogenation of allyl alcohol over an amorphous copper-zirconium alloy. *Journal of Molecular Catalysis A: Chemical,* 112, 85-92.

Mckinsey Report (No Date), A portfolio of power-trains for Europe: a fact-based analysis – The role of battery electric vehicles , plug-in hybrids and fuel cell electric vehicles, [PDF – Accessed on 20th November 2012].

Nenoff, T. M., Spontak, R. J., Editors, G., & Aberg, C. M. (2006). Membranes for Hydrogen Purification : An Important Step toward a Hydrogen- Based Economy. *MRS Bulletin*, *31*(October).

Ockwig, N. W., & Nenoff, T. M. (2007). Membranes for hydrogen separation. *Chemical reviews*, *107*(10), 4078-110. doi:10.1021/cr0501792.

Okamoto, H. (2008). Cu-Zr (copper-zirconium). *Journal of Phase Equilibria and Diffusion*, *29*(2), 204-204.

Paglieri, S. N., Birdsell, S. A., Barbero, R. S., Snow, R. C., & Smith, F. M. (2006). *U.S. Patent No. 7,022,165*. Washington, DC: U.S. Patent and Trademark Office.

Paglieri, S. N., & Way, J. D., (2002), Innovations in palladium membrane research. *Separation Purification Reviews*, 31.1: 1- 169.

Patterson, E., (2011), Better fuel cell membrane materials, [online], Available from: http://www.lanl.gov/science/1663/november2010/story8.shtml, [Accessed on 10th January 2013].

Peachey, N. M., Snow, R. C., & Dye, R. C. (1996). Composite PdTa metal membranes for hydrogen separation. *Journal of Membrane Science*, *111*(1), 123-133. doi:10.1016/0376-7388(95)00298-7.

Peng, D. L., Yan, M., Sun, J. F., Shen, J., Chen, Y. Y., & McCartney, D. G. (2005). Enhanced thermal stability by pre-charged hydrogen of a Zr-based bulk metallic glass. *Journal of alloys and compounds*, *400*(1), 197-201.

Phair, J. W., & Badwal, S. P. S. (2006). Materials for separation membranes in hydrogen and oxygen production and future power generation. *Science and Technology of Advanced Materials*, *7*(8), 792-805. doi:10.1016/j.stam.2006.11.005.

Piper, J., (1965) Diffusion of hydrogen in copper-palladium alloys, *Journal of Applied Physics*, 37(2).

Prosperi, D., (2006), Investigation of palladium/stainless-steel membranes for use in H_2 separation applications. Department of Metallurgy and Materials, University of Birmingham.

Riis, T., Hagen, E. F., Vie, P. J., & Ulleberg, Ø. (2005). Hydrogen Production–Gaps and Priorities. *IEA hydrogen implementing agreement.*

Rubin, S. E., Anand R. B., & Chen, C., (2004), Comparative assessments of fossil fuel power plants with CO_2 capture and storage. *Proceedings of 7th International Conference of Greenhouse Gas Control Technologies (GHGT-7), Vancouver, Canada, September 5-9.*

Sakamoto, Y., Baba, K., Kurashashi, W., Takao, K., & Takayama, S. (1984). Diffusion of Hydrogen in some Amorphous Alloys. *Journal of Non-Crystalline Solids*, *62*, 691-696.

Shen, Y. T., Xing, L. Q., & Kelton, K. F. (2005). Formation and crystallization of ZrCuTi metallic glasses. *Philosophical Magazine*, *85*(31), 3673-3682.

Shimpo, Y., Yamaura, S.-I., Nishida, M., Kimura, H., & Inoue, A. (2006). Development of melt-spun Ni–Nb–Zr–Co amorphous alloy for high-performance hydrogen separating membrane. *Journal of Membrane Science*, *286*(1-2), 170-173. doi:10.1016/j.memsci.2006.09.031.

Sholl, D. S. & Hao S., (2011). Computational prediction of durable amorphous metal membranes for H2 purification. *Journal of Membrane Science*, *381*(1-2), 192-196. Elsevier B.V. doi:10.1016/j.memsci.2011.07.026.

Sholl, D. S., & Ma, Y. H. (2006). Dense Metal Membranes for the Production of High-Purity Hydrogen. *MRS Bulletin*, *31*(October), 770-773.

Sigma Technologies (2012), Purification technologies – Palladium membrane purification, [online], Available from: http://www.sigma-tech.it/tec_palladium.asp, [Accessed on 12th January].

Spiegel Online International, (2011), Crossing the 20 percent mark: Green energy use jumps in Germany, [online], Available from: www.spiegel.de/international/crossing-the-20-percent-mark-green-energy-use-jumps-in-germany-a-783314.html, [Accessed on January 25th 2013].

Spillman, R. W. (1989). Economics of gas separation membranes. *Chemical Engineering Progress*, *85*(1), 41-62.

Strom-Olsen, J., Zhao, Y., Ryan, D., Huai, Y., & Cochrane, R. (1991). Hydrogen diffusion in amorphous Ni-Zr. *Journal of the Less Common Metals*, *172-174*, 922-927. doi:10.1016/0022-5088(91)90221-O.

Tang, H., Ishikawa, K., & Aoki, K. (2008). Microstructure, Ductility and Hydrogen Permeability of Nb-Ti-Zr-Ni Alloys. *Materials Transactions*, *49*(10), 2220-2223. doi:10.2320/matertrans.MA200808.

Tong, H, D., Gielens, F. C,. Gardeniers, J. G. E, Jansen, H. V., van Rijn, C. J. M, Elwenspoek, M. C., & Nijdam, W., (2004), Microfabricated palladium-silver alloy membranes and their application in hydrogen separation. *Industrial & Engineering Chemistry Research*, *43* (15), 4182-4187.

U.S. Energy Information Administration, U.S. Department of Energy (DOE) Monthly energy review DOE 2013, Available at [http://www.eia.gov/totalenergy/data/monthly/pdf/mer.pdf] Accessed on 21st January 2013).

Van Delft, Y. C., Correia, L. A., Overbeek, J. P., Bongers, B., & Pex, P. P. A C., (2006), Hydrogen transport through thin layer palladium membranes: kinetics and gas permeation studies. *Presented at the 9th International Conference of Inorganic Membranes - ICIM-9, 25 – 29 June*, Lillehammer, Norway.
Wang, Y. I., Suh, J. Y., Lee, Y. S., Shim, J. H., Fleury, E., Whan Cho, Y., & Koh, S. U. (2013). Direct measurement of hydrogen diffusivity through Pd-coated Ni-based amorphous metallic membranes. *Journal of Membrane Science*.

Wang, H. R., Ye, Y. F., Shi, Z. Q., Teng, X. Y., & Min, G. H. (2002). Crystallization processes in amorphous Zr< sub> 54</sub> Cu< sub> 46</sub> alloy. *Journal of non-crystalline solids*, *311*(1), 36-41.

Wei, I. W., & Brewer, J., (1996), Desorption of hydrogen from palladium plating. *AMP Journal of technology* 5 (1996).

Wicke V. E., & Nernst G. H., (2010) Zustandsdiagramm und thermodynamisches Verhalten der Systeme Pd/H_2 und Pd/D_2 bei normalen Temperaturen; H/D-Trenneffekte. *Berichte der Bunsengesellschaft fur physikalische Chemie*, 68(3), 224 – 235.

Yamanaka, S., Yamada, K., Kurosaki, K., Uno, M., Takeda, K., Anada, H., ... & Kobayashi, S. (2001). Thermal properties of zirconium hydride. *Journal of nuclear materials*, *294*(1), 94-98.

Yamaura, S. I., Nakata, S., Kimura, H., Shimpo, Y., Nishida, M., & Inoue, A., (2005), Hydrogen permeation of the melt-spun Ni-X-Zr amorphous membranes. *Materials transactions*, 46(8), 1768.

Yamaura S., Shimpo Y., Okouchi H., Nishida M., Kajita O., & Inoue A., (2004) The effect of additional elements on hydrogen permeation properties of melt-spun Ni-Nb-Zr amorphous alloys, *Materials Transactions*, 45 (2), 330-333.

Yun S., & Oyama T., (2011) Correlations in palladium membranes for hydrogen separation: A Review, *Journal of Membrane Science*, 375, 28-45.